Science Advances
AAAS

Supplementary Materials for

Cellular costs underpin micronutrient limitation in phytoplankton

J. Scott P. McCain*, Alessandro Tagliabue*, Edward Susko, Eric P. Achterberg, Andrew E. Allen, Erin M. Bertrand*

*Corresponding author. Email: j.scott.mccain@dal.ca (J.S.P.M.); a.tagliabue@liverpool.ac.uk (A.T.); erin.bertrand@dal.ca (E.M.B.)

This PDF file includes:

Model Parameters
Supplementary Methods
Supplementary Discussion
Supplementary Figures
Table S1
Algorithm 1
Figs. S1 to S16
References

1 Model Parameters

Table S1. Mathematical symbols, names, units, numerical values, and detailed descriptions for all the parameters in the proteomic allocation model described in the main text.

Parameter Symbol	Parameter Name	Units	Value	Description
$\eta_{T_{NO_3}}$	Nitrogen Metabolism Protein Complex Size	$\frac{AminoAcids}{Molecule}$	5893	There are nine NRT2 transporters found in the *F. cylindrus* genome. The average length is 512. There are three proteins in the *F. cylindrus* genome that are associated with the GO term 'Nitrate reductase activity'. After pBLAST, these proteins were further identified as one nitrate reductase and two cytochrome b5. There is one cytochrome b5 domain in nitrate reductase, and nitrate reductase also functions as a homodimer. We take the average length of the two cytochrome b5 proteins (136 and 122 amino acids), added with the nitrate reductase protein length (862), to a amino acid total of 991 (multiplied by two, 1982). There are four enzymes associated with nitrite reductase activity (three with ferredoxin-nitrite reductase and one with NADPH dependent nitrite reductase). We took the average length of all NiR proteins (832 amino acids). There are five proteins in the *F. cylindrus* genome that associate with the GO term 'Glutamine biosynthetic process' (GO Term: 0004356). After pBLAST, two appear to be glutamine synthetase/quinado kinase, two are plastid glutamine synthetase II, and one is glutamine synthetase type. The average protein length is 450. Glutamine is converted to glutamate by glutamate synthase, and we found 10 proteins with 'glutamate synthase activity' via GO terms. These proteins were then searched using pBLAST, and of them, there were four hypothetical proteins, two FMN-linked oxidoreductases, two 'glutamate synthase family proteins', one glutamate synthase (NADPH) large chain protein, and one NADH-glutamate synthase small subunit. We took the average length of the glutamate synthase family proteins and large subunit (1596), and summed it with the small subunit protein (521), to a total of 2117 amino acids. The total amino acid count fo protein complex size is $512 + 1982 + 832 + 450 + 2117 = 5893$.

η_R	Ribosome protein complex size	$\frac{AminoAcids}{Molecule}$	28800	96 proteins estimated for cytosolic ribosomes in *Chlamydomonas reinhardtii* (*81*). These proteins range in size from 12-54kDa. Assuming an average size of 33kDa, this converts to a protein cost of 3168kDa (3168000Da), or 28800 amino acids (assuming an average of 110 Da per amino acid).
$\eta_{T_{Mn,Unadjusted}}$	Manganese uptake protein complex size	$\frac{AminoAcids}{Molecule}$	372	There are four NRAMPs identified in the *F. cylindrus* genome (protein ID 137845, 173050, 172829, 197170) and subsequently checked with BLASTp and confirmed to be divalent metal tranporter 1 or an NRAMP. The average protein size is (422, 314, 398, 355 for the above protein IDs, respectively) is 372.

| $\eta_{T_{Fe,Unadjusted}}$ | Iron uptake protein complex size | $\frac{AminoAcids}{Molecule}$ | 4030 | GO:0006826 (iron ion transport) was used. Ferritin (protein ID 249610, 201 amino acids), iron permease FTR1 family (PF03239; protein ID 243554, 371 amino acids), ISIP1 (protein ID 241515, 594 amino acids) (ISIPs included because of putative role in iron transport and ubiquitous role in iron response), protein ID 236396 (102 amino acids), periplasmic ABC transporter (GO:0005381 iron ion transmembrane transporter activity, GO:0006827 high-affinity iron ion transmembrane transport; protein ID 193804, 301 amino acids, protein ID 195906, 206 amino acids, protein ID 197108 301 amino acids, protein ID 202747 207 amino acids, protein ID 172711 1733 amino acids, not included because sequence gaps impacts gene model), iron transporter Ferroportin1 (PF06963) protein ID 147624 493 amino acids, ABC transporter periplasmic Fe3+ hydroxamate transport system (protein ID 209416, 348 amino acids), ZIP Zn/Fe transporter (KOG1558, protein ID 184218 296 amino acids, protein ID 268016 179 amino acids), Ferric reductase / NADH/NADPH oxidase and related proteins (Protein ID 232972 824 amino acids, Protein ID 246292 917 amino acids, Protein ID 259423 1321 amino acids, Protein ID 227601 761 amino acids, Protein ID 235878 818 amino acids, Protein ID 252645 599 amino acids, Protein ID 184052 728 amino acids), sideroflexin (protein ID 140510 367 amino acids, Protein ID 216838 290 amino acids, Protein ID 226433 347 amino acids). The sum of all these proteins is 201 + 371 + 594 + 102 + mean(c(301, 206, 301, 207)) + 493 + 348 + mean(c(296, 179)) + mean(c(824, 917, 1321,761, 818, 599, 728)) + mean(c(367, 290, 347)) = 3787. We exclude Ferritin (201 amino acids), as we explicitly include this protein elsewhere. We also include the four copies of FBP1 identified by (*83*), in *F. cylindrus*, which have the average length of 442 (556, 235, 531, 449) thus the final cost is 4029 (rounded to 4030 in the model). |
| η_P | Photosystem unit size | $\frac{AminoAcids}{Molecule}$ | 12177 | Data from (*82*), and we assume a 1:1 ratio of PSII:PSI. |

η_A	Manganese superoxide dismutase size	$\frac{AminoAcids}{Molecule}$	227	Protein ID 185706 (232 amino acids), 239458 (223 amino acids). GO:0004784, GO:0006801.
θ	Dynamic Fe uptake cost coefficient	$\frac{AminoAcids}{Fe}$	1.469	Determined using Approximate Bayesian Computation.
θ	Dynamic Mn uptake cost coefficient	$\frac{AminoAcids}{Mn}$	1.469	Determined using Approximate Bayesian Computation.
r	Radius	Metres	0.000003952	Inferred from Figure 1a in ref. (*24*).
s	Transporter complex radius	Metres	1.00E-09	From ref. (*63*).
M_{Cell}	Amino acids per cell	$\frac{AminoAcids}{Cell}$	1.4E+11	From ref. (*77*), data from Supplementary File S1. The median picograms of protein per cell from *Pseudo-nitzschia* (*Fragilariopsis cylindrus* not in dataset) was 15.53692pg. Converted to grams per cell (1/1e12), then to amino acids per cell.
Λ	Proportion of the proteome that is independent of growth rate	Dimensionless	0.2	Estimated using calculations from (*79*).
κ	Available space on the membrane for Mn and Fe transporters	Dimensionless	0.1484	Determined using Approximate Bayesian Computation.
m_γ	Energy use per amino acid elongation	$\frac{e}{AminoAcid}$	3	From ref. (*25*).
φ_N	Energy use per NO_3 conversion into amino acids	$\frac{e}{NO_3}$	9.8	1 ATP for import + 1 NADPH for nitrate reduction + 1 NADPH for nitrite reduction + 1 ATP for glutamine synthetase + 1 NADPH for glutamate synthase. Assuming an interconversion ratio of 2.6 ATP to 1 NADPH, the total cost is: 1ATP + 2.6ATP + 2.6ATP + 1ATP + 2.6ATP = 9.8e.
$\varphi_{Fe,P}$	Iron per PSU	$\frac{Fe}{PhotosystemUnit}$	20	From ref. (*106*).
$\varphi_{Fe,N}$	Iron per N uptake and synthesis	$\frac{Fe}{NitrogenPathway}$	10	2 Fe in nitrate reductase (one per subunit, but it exists as a homodimer), 5 Fe in nitrite reductase in total (1 siroheme cofactor and 4 in 4Fe-4S cluster), 3Fe in glutamate synthase. Total is 10 Fe.
$\varphi_{Mn,A}$	Manganese per MnSOD	$\frac{Mn}{MnSOD}$	1	From ref. (*107*).
$\varphi_{Mn,P}$	Manganese per PSU	$\frac{Mn}{PhotosystemUnit}$	4	From ref. (*106*).

φ_e	Energy produced per PSU activation	$\frac{e}{PSU\,Activation}$	8	From ref. (25).
$\varphi_{T_{Mn}}$	Energy used for Mn uptake	$\frac{e}{Mn}$	2	Set to an arbitrarily low value to ensure Mn uptake is not possible with zero energy.
$\varphi_{T_{Fe}}$	Energy used for Fe uptake	$\frac{e}{Fe}$	2	Set to an arbitrarily low value to ensure Fe uptake is not possible with zero energy.
m_n	Inverse of nitrogen per amino acids	$\frac{AminoAcid}{Nitrogen}$	6.99E-01	Averaged across all amino acids.
k_{cat,T_N}	Maximum turnover rate of the rate-limiting enzyme in the nitrogen assimilation pathway	$\frac{1}{minute}$	178	At substrate saturating conditions, the enzyme with the lowest maximum turnover rate in a pathway determines the upper bound on flux through the pathway, assuming constant total amount of a enzyme (as it is represented in the model as an entire protein pool). Nitrate reductase is sometimes referred to as the rate limiting step in nitrogen assimilation ($k_{cat} = 12\ \frac{1}{second}$ in spinach). (108) estimated the nitrate reductase k_{cat} equal to $20\ \frac{1}{second}$ in *Arabidopsis thaliana*. We note that for glutamine synthetase, there was a lower k_{cat} for NH_4^+ at $2.96\ \frac{1}{second}$. We therefore used this as the rate limiting step in nitrogen assimilation to amino acids.
γ_{max}	Protein synthesis rate	$\frac{AminoAcids}{Minute \cdot Ribosome}$	1.14E+02	*Thalassiosira weissflogii* translation rate at 20 C is $1.9\ \frac{AminoAcid}{Ribosome \cdot second}$. Assuming a temperature depence given by a factor of $Q_10 = 2$ (18), protein synthesis rate is adjusted in the model. (Protein synthesis rate temperature adjusted $= 114 \cdot 2^{(T/10-20/10)}$, where T is temperature and equal to -1 C).
$k_{cat,Fe}$	Maximum turnover rate, Fe transporter	$\frac{1}{Minute}$	352	Discussed in text. (70) values, using (38) calculation of handling time.
$k_{cat,Mn}$	Maximum turnover rate, Mn transporter	$\frac{1}{Minute}$	352	Kinetic constants for Fe uptake are assumed to be equivalent to Mn transporters, but further work is required for distinct parameterizations across micronutrients.

$k_{cat,ROS}$	Maximum turnover rate, Mn-SOD	$\frac{1}{Minute}$	10000	Taken from a range of BRENDA Database of kinetic constants for superoxide dismutases and from other publications (lower end was conservatively chosen consistent with argument from (33), as a lesser efficiency would correspond with more demand, and a higher potential interaction between MnSOD production and oxidative stress). Note that this parameter is multiplied in the model by ϵ_a, making it have a more phenomenological interpretation.
$K_{Fe_i,P}$	Half saturation constant for Fe_i to Photosystems	$\frac{Molecules}{Cell}$	10000	Set to an arbitrarily low value.
$K_{Mn_i,P}$	Half saturation constant for Mn_i to Photosystems	$\frac{Molecules}{Cell}$	10000	Set to an arbitrarily low value.
$K_{Mn_i,A}$	Half saturation constant for Mn_i to Antioxidants	$\frac{Molecules}{Cell}$	10000	Set to an arbitrarily low value.
$K_{Fe_i,N}$	Half saturation constant for Fe_i to Tn (N uptake and biosynthesis)	$\frac{Molecules}{Cell}$	10000	Set to an arbitrarily low value.
K_e	Half saturation constant for energy	$\frac{Molecules}{Cell}$	10000	Set to an arbitrarily low value.
ϵ_a	Efficacy per MnSOD	Dimensionless	0.00001	Determined using Approximate Bayesian Computation.
σ	Absorption Cross Section	$\frac{m^2}{uE}$	0.01	From ref. (87).
τ	Activated photosystem turnover rate	$\frac{1}{Minute}$	6000	We obtained the values from the mean shown in Figure 2E for phytoplankton in (88), of 0.1 ($\frac{1}{ms}$). Converting to minutes, this results in an value of 6000 ($\frac{1}{Minute}$).
R_0	Shape of the ROS mismatch penalty function	Dimensionless	10	Arbitrarily chosen.

2   Supplementary Methods

2.1   Optimization

Our model optimizes the set of parameters that describe the proportion of ribosomes translating for a given protein pool ($\vec{\beta}$), and we used the steady-state growth rate as the objective function (*25*). We used several techniques to improve the accuracy and speed of optimization.

The computational problem can be broken down into two stages. The first stage is solving for the steady state growth rate, and the second stage is determining which set of parameters lead to the optimal growth rate. We chose to set up the first problem as a system of ordinary differential equations (ODEs), and numerically integrate these ODEs to a pseudo-steady state (*25*). The rates within the ODEs are a function of the proportion of ribosomes translating each proteomic pool ($\vec{\beta}$). So, in order to determine the optimal $\vec{\beta}$ we need integrate the system of ODEs to a steady state to evaluate the growth rate (μ). To perform the numerical integration, we used the python module SciPy *odeint*, which accesses the LSODA algorithm in ODEPACK (*109*). The integration time step varied, depending on whether it was used for the ABC analysis or the parameter perturbation experiments. However, the maximum number of internally defined time steps (*mxstep* in *odeint*) was kept at 1E6.

In order to determine the optimal $\vec{\beta}$, we used Sequential Least Squares Quadratic Programming (SLSQP, SciPy), a method used for non-linear, constrained, and bounded optimization problems. However, we found that the minimization was highly start-point dependent due to the nature of the optimization problem. We developed a three-component optimization protocol to approach this problem. In the first component ('the drunkards walk'), we used SLSQP initialized with a random $\vec{\beta}$ with a high error tolerance, performed n times. For all model experiments (parameter perturbations), and for the baseline model, we set this value to $n = 20$. For running the ABC, we used $n = 10$, because it is slightly faster. During this stage, the integration time for determining the steady-state growth rate was set to 5E5 (with a time step of 10). The 'high error' tolerance corresponded with a value of 1E-4 for the *ftol* parameter in SciPy minimize, which is the precision goal for the growth rate value in the stopping criterion. We also set the maximum iterations parameter (*maxiter*) to 200 for the minimize function in SciPy. For all other parameters we used default settings.

The second component is an empirical Bayesian optimization using Gaussian Process Regression, informed from the original set of n random guess. Conceptually, this approach is improving the sampling of parameter space because it is not dependent on randomly generated $\vec{\beta}$, but a guided search. After the first component, we use the SLSQP determined $\vec{\beta}$, paired with their steady state growth rates, to train a Gaussian Process Regression (GPR) model. We use this approach because evaluating our objective function is computationally expensive. The GPR model covariance function is an additive combination of the dot product and White kernel. Once we have trained the GPR model, we generate p random $\vec{\beta_P}$, evaluate all $\vec{\beta_P}$ using the trained GPR model, and then determine which $\vec{\beta_P}$ would have the highest growth rate. For all model experiments and the baseline model runs, we set $p = 1000$. For the ABC analysis, we set $p = 300$. We then use the top 20% p values (as ranked by their GPR-predicted μ) as initial starts for the SLSQP approach. After these $\vec{\beta}$ values are evaluated with the objective function, we re-train the GPR model with these additional observations k times. For all model experiments and baseline model runs, we set $k = 10$, for the ABC analysis we set $k = 2$.

The third component is a refined optimization with lower error tolerance ('the sober walk'). We begin by taking the top 10% of $\vec{\beta}$, ranked by their growth rate. From this sub-group, we use a k-means clustering of these parameter sets. We then take the j centroids from the k-means clustering, and use these as inputs for the 'sober walk'. This last component uses the k-means clustering centroids as start points for the SLSQP optimization, with a lower error tolerance compared to above. The 'low error' tolerance corresponded with a value of 1E-6 for the *ftol* parameter in SciPy minimize. The optimal $\vec{\beta}$ is the parameter set, from this component, which resulted in the highest steady-state growth rate.

We found that these steps above improved both the computational speed and accuracy of the optimization. Additionally, we used the square-root of the growth rate, which flattens the optimization surface and we found to improve the accuracy of our optimization. We also used a shorter steady-state time during the 'drunkards walk', which is a good approximation of the steady state growth rate, but it is much more efficient because the time-length of integration is much smaller.

Algorithm 1: Optimization algorithm description. n is the number of initial random parameter guesses. ϵ_f is fixed proteomic fraction. SLSQP: Sequential Least Squares Quadratic Programming, a constrained optimization protocol.

Result: $\vec{\beta_{Opt}}$
for n **do**

    Generate random $\vec{\beta}$ such that $\sum_j \beta_j = 1$;

    High error tolerance SLQSP using $\vec{\beta}$ as initial value and $\sqrt{\mu}$ as objective function;

    Generate initial optimized $\vec{\beta_i}$ and corresponding μ_i;

end

Train a Gaussian Process Regression (GPR) model using all $\vec{\beta_i}$ and corresponding μ_i;

for k **do**

    Generate p, $\vec{\beta_p}$ such that $\sum_j \beta_j = 1$;

    for p **do**

        | Predict μ using trained GPR;

    end

    Subset which $\vec{\beta_p}$ had the highest GPR-predicted μ;

    Evaluate these subsetted $\vec{\beta_p}$ using a high error tolerance SLQSP, determine corresponding μ_p;

    Re-train GPR model with new, appended set of $\vec{\beta_p}$ and corresponding μ_p;

end

K-means clustering of top 10%, ranked by μ.

for i **do**

    Low error tolerance SLQSP using K-means cluster centroids as initial values and $\sqrt{\mu}$ as objective function;

end

---

3 Supplementary Discussion

3.1 Model parameter posteriors interpretation

We estimated three key, unconstrained model parameters, each corresponding to different cellular processes: (1) internal Fe protein cost, (2) available membrane space for transporters, and (3) the catalytic efficiency of MnSOD. Below we provide a detailed discussion of their interpretation. The first parameter represents the strength of this internal cost in our model by multiplying the cellular Fe quota by a coefficient, which is interpretable as the amino acids required for managing each Fe atom. If all Fe was bound to ferritin, for example, this coefficient would be the total amino acids per ferritin protein complex divided by the total amount of Fe per ferritin protein complex. This parameter significantly increases the protein cost per transporter.

The second key parameter was the available membrane space for Mn and Fe transporters. Note that our estimate of available membrane space corresponded with the upper-bound of our prior distribution for this parameter – a wider prior distribution may have resulted in a higher value. We chose this upper bound (15% of membrane surface area) because approximately 50% of the membrane can be allocated to proteins to maintain lipid bilayer integrity (*68*). There is also a membrane requirement for macronutrient transporters (e.g. phosphate, nitrate, or silicate). We therefore reasoned that Fe and Mn transporters took up a maximum of 15% of the membrane space. Yet, targeted work on membrane protein dynamics, particularly in eukaryotic phytoplankton, is clearly required to obtain a more accurate upper bound for available area for membrane transporters.

The last unconstrained parameter was the catalytic efficiency of MnSOD. Superoxide dismutases are incredibly efficient enzymes (*107*). If we constructed this model to simply minimize steady-state concentrations of superoxide (assuming a well mixed compartment), only a few copies of MnSOD would be required. Yet, that is not observed in field-based proteomes (our data presented here) or in cultured diatoms (e.g. *45*). There is also evidence that MnSOD is associated with the chloroplastic membrane directly suggesting some degree of producing this critical protein at levels higher than would be suggested from kinetic-based reasoning (*110, 111, 112*). In other words, an overproduction of MnSOD would prevent free superoxide from diffusing and interacting with biomolecules. Yet, the *degree* of overproduction is uncertain – this is one way this parameter may be interpreted.

3.2 Iron-light interactions in the Southern Ocean

Recently, some evidence suggesting that Southern Ocean phytoplankton have a unique relationship between Fe and light levels has emerged, which is mediated by low temperatures (*88*). We predicted an inverse relationship between light levels and cellular Fe quotas, consistent with previous work (*49*). It is unsurprising that we do not predict the relationship observed in ref. (*88*), as it was not included within our photosynthetic model. Future work is required to address how various temperature-dependent mechanisms (e.g. photosynthetic processes, translation rate, Fe uptake kinetics, membrane saturation, etc.) integrate to influence the complex relationship between Fe, Mn, temperature, and light.

3.3 Iron and manganese interactions

A key mechanism of interdependence between Mn and Fe was included in our model (*33*). Briefly, under low Fe, electrons leak more from electron transport, increasing the requirement for MnSOD. Therefore, under low Fe, Mn should have a relatively larger impact on growth rate than at high Fe. Despite explicitly including an interaction between Mn and Fe in our model, we found that these two micronutrients influenced growth rate mostly independent of each other.

Antioxidants are produced to counteract ROS production via leaked electron flux. There are two controls on total leaked electron flux: 1) the proportion of electrons leaked and 2) the total electron flux. Low Fe increases the proportion of electrons leaked, but it also decreases the total electron flux. Therefore, while the requirement of MnSOD *per PSU* increases under low Fe, the total requirement for MnSOD decreases. These observations challenge the result that Fe and Mn interact under low Fe – seemingly inconsistent with the observed increase in Mn quota under low Fe (*33*). However, several lines of evidence from ref. (*33*) are actually consistent with our predictions and newer observations. Our model also predicts an increase in Mn quota under low Fe, yet the source of this increased quota is an increased internal free Mn pool, not MnSOD. Increased reactive oxygen species observed under low Fe (*33*) is consistent with superoxide secreted to increase bioavailability of ligand-bound Fe (*113*), or with a recently discovered mechanism relating superoxide production with photosynthetic health (*114*). Our model results suggest that Mn actually has a larger role in influencing growth rate under high Fe, rather than low Fe, and a reframing of previous growth rate data provides some support for this conclusion (Supplementary Fig. S9). Yet, these geochemical conditions are infrequently encountered in the Southern Ocean (Supplementary Fig. S2), so it is unclear how much Mn and Fe interact to control phytoplankton growth in the Southern Ocean. Furthermore, it is unclear how to reconcile observations suggesting Mn limits primary productivity (*26, 27, 28, 115, 116*). Perhaps a more complex, community-interaction is at play, or other organisms (e.g. haptophytes) are contributing to this phenomenon.

3.4 Proteomic allocation model predictions compared with field-based diatom proteomes

Our model captures trends in fold change for most protein pools from the two weeks with both proteomic observations and geochemical data. It did not capture the trends in expression of nitrogen metabolism and uptake, and antioxidants. We observed a decrease in photosystem units (PSUs) and ribosomes from Week 1 to Week 3 in both the experimental metaproteomic time series (dotted vertical lines, Supplementary Fig. S12) and the model predictions. However, the model did not capture the trend in abundance change for the nitrogen metabolism protein pool. We hypothesize that the lack of correspondence is because our model only considers nitrogen uptake from nitrate, whereas concurrent experiments suggested diatoms were using ammonium (*40*), which is more Fe efficient (*117*). The posterior distribution for antioxidant expression did not clearly indicate one direction of expression (i.e. increase or decrease). Thus, more targeted work examining the expression of this key protein pool is required.
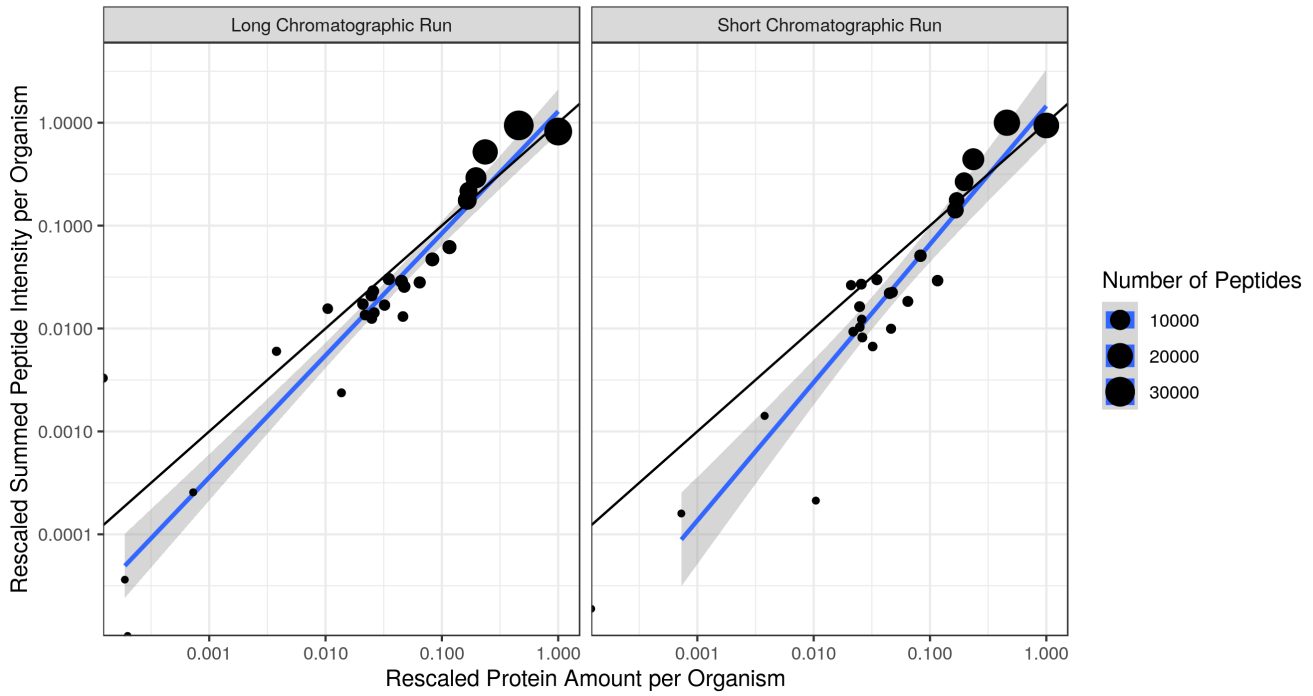
4 Supplementary Figures

Figure S1: Correlation between sum of taxon-specific peptide intensities per taxonomic group and total protein used for each taxa using the ref. *42* artificial metaproteome. The sum of peptide intensities per group is a valid proxy of biomass across both the 'Long' and 'Short' chromatographic runs (right and left panels). Values from both axes are rescaled such that they vary from 0–1. The 1:1 line of y = x is plotted in black, and the blue line represents a linear model. Point size reflects the number of peptides observed for a given taxa.
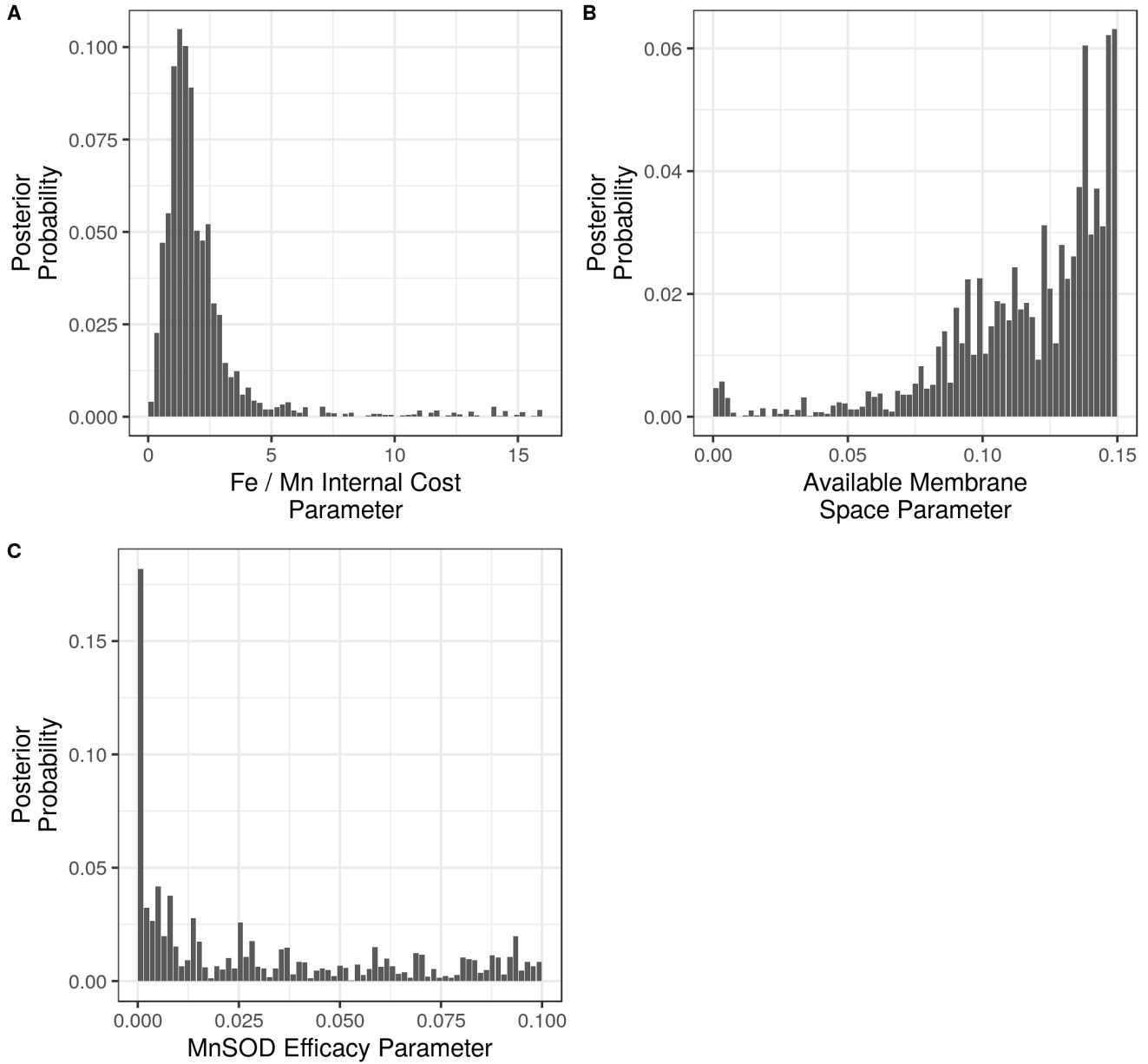
Figure S2: Posterior probability distributions for each of the three unconstrained, estimated parameters. Parameters were estimated using Approximate Bayesian Computation (see Methods). The modes of each distribution were used for the inferred parameter value. Each bar represents the posterior probability for a given cellular parameter within that interval (Methods).
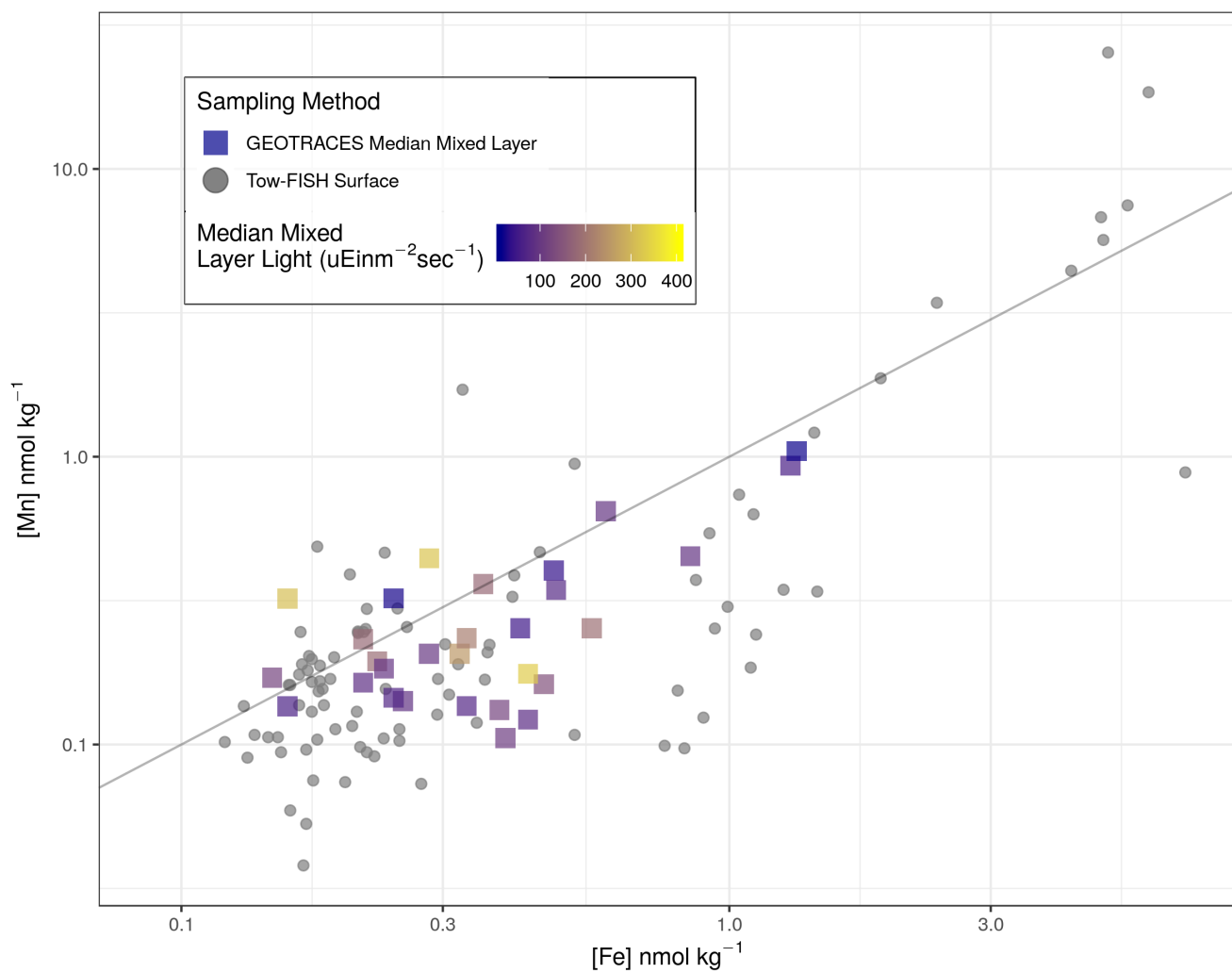
Figure S3: Southern Ocean concentrations of dFe and dMn from two data sources (Methods). Circles represent concentrations derived from a surface Tow-FISH on GEOTRACES cruise JR274. Squares are median mixed layer concentrations of dMn and dFe from GEOTRACES cruises in the Southern Ocean, GEOTRACES Intermediate Data Product *92*. Corresponding light levels were calculated using the Ocean Color database (*118*).
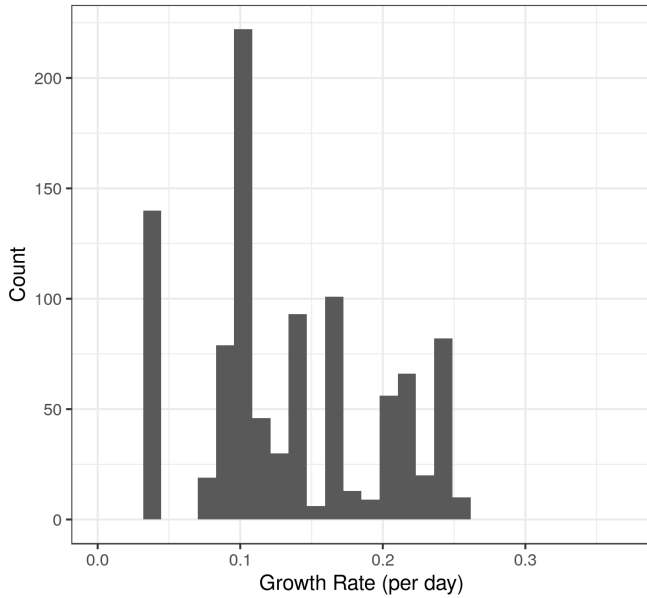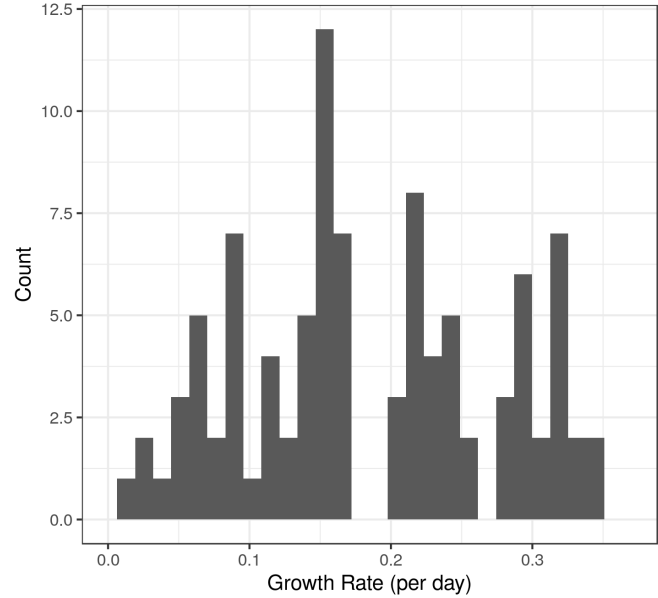
Figure S4: Histogram of growth rates from the cellular model (left, 1–3000 pM dFe, 1–3000 pM Mn) are within the same range of observed growth rates of *Fragilariopsis cylindrus* across a range of iron and temperatures (*40*).
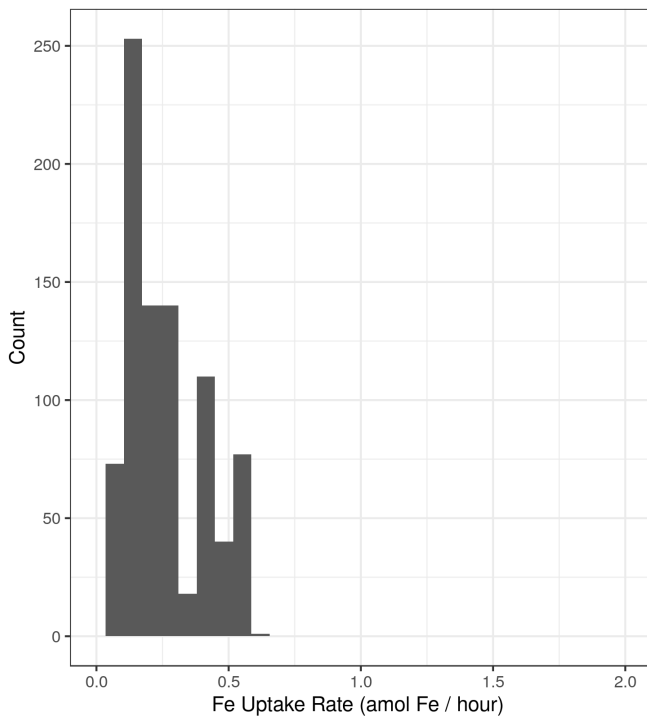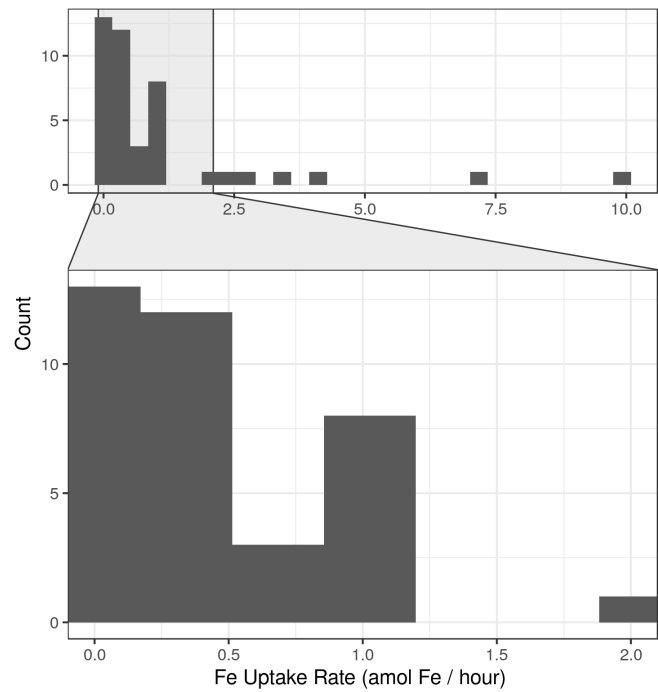
Figure S5: Histogram of Fe uptake rates from the cellular model (left, 1–3000 pM dFe, 1–3000 pM Mn) are within the observed range of Fe uptake rates of *Phaeodactylum tricornutum* (*48*).

A Model Fe Quota (histogram)
Observed Fe Quota (Peers and Price, 2004; dotted lines)
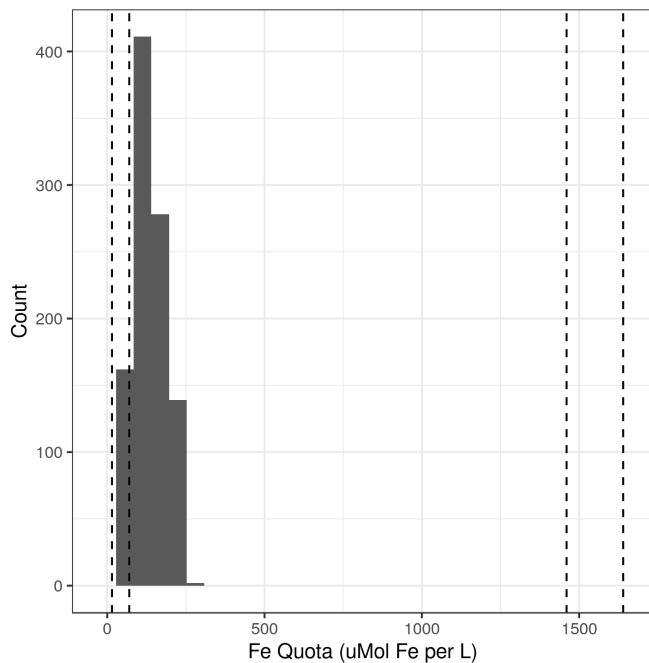
B Model Mn Quota (histogram)
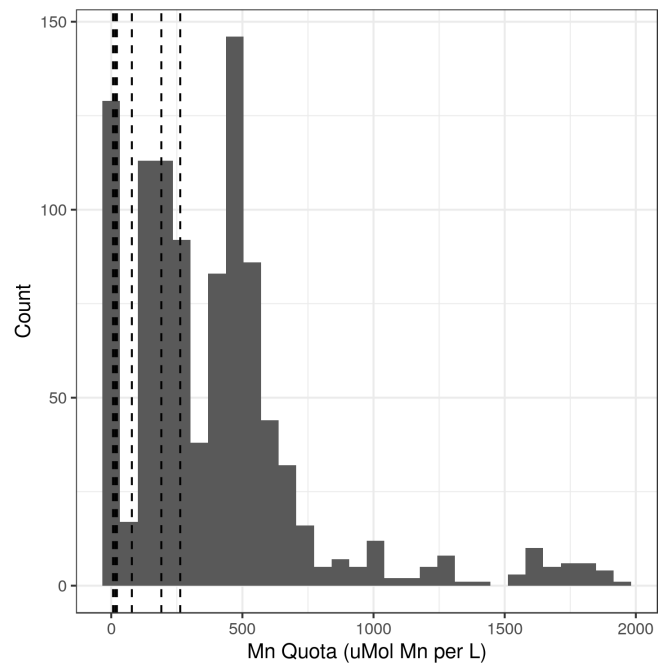Observed Mn Quota (Peers and Price, 2004; dotted lines)

Figure S6: Model Fe and Mn quotas (histograms, 1–3000 pM dFe, 1–3000 pM dMn) overlap with the observed range of cellular quotas from *Thalassiosira pseudonana* (dotted lines, *33*).
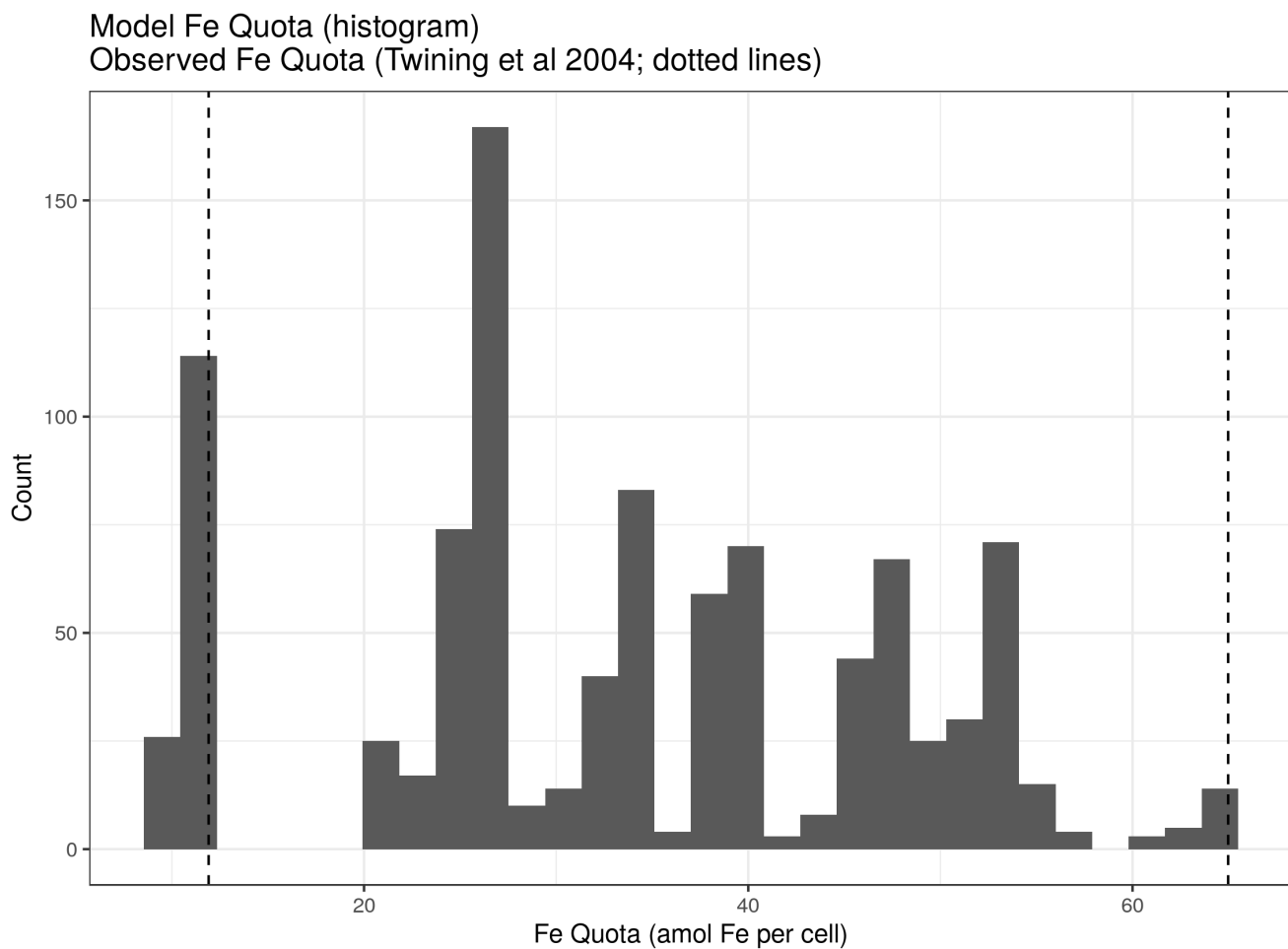
Figure S7: Model Fe and Mn quotas (histograms, 1–3000 pM dFe, 1–3000 pM dMn) overlap with the observed range of cellular quotas from diatoms collected on the SOFeX expedition to the Southern Ocean (dotted lines, *47*).
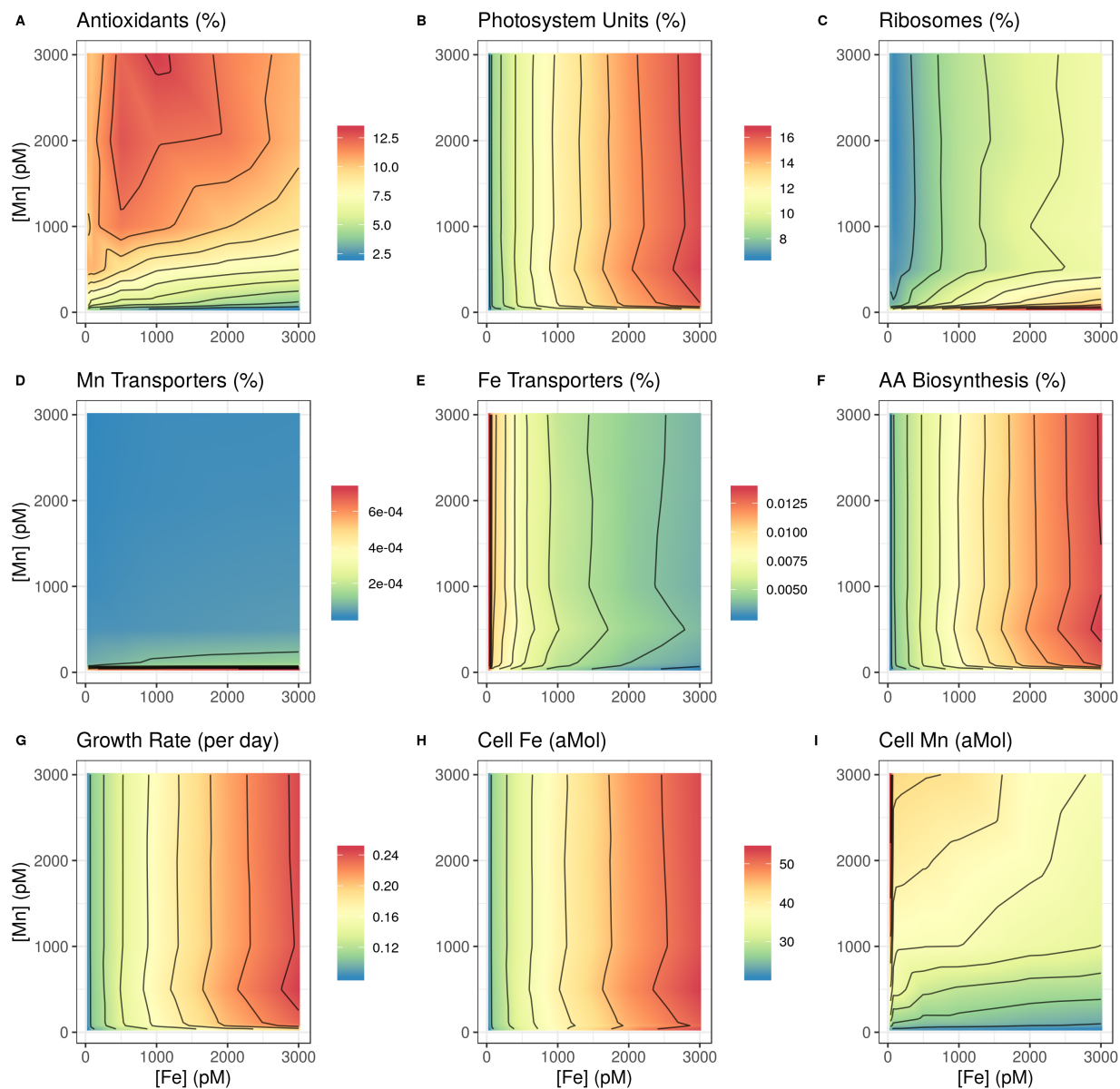
Figure S8: Model runs across a wide range of iron and manganese concentrations typically observed in the Southern Ocean. Light levels were 50 $\mu Einm^{-2}s^{-1}$. (**A-F**), proteomic mass fractions for each proteomic pool from the cellular model. (**G**), growth rate across a wide range of Fe and Mn concentrations. (**H-I**), total cellular quotas of Fe and Mn, including the free Mn and Fe pools.
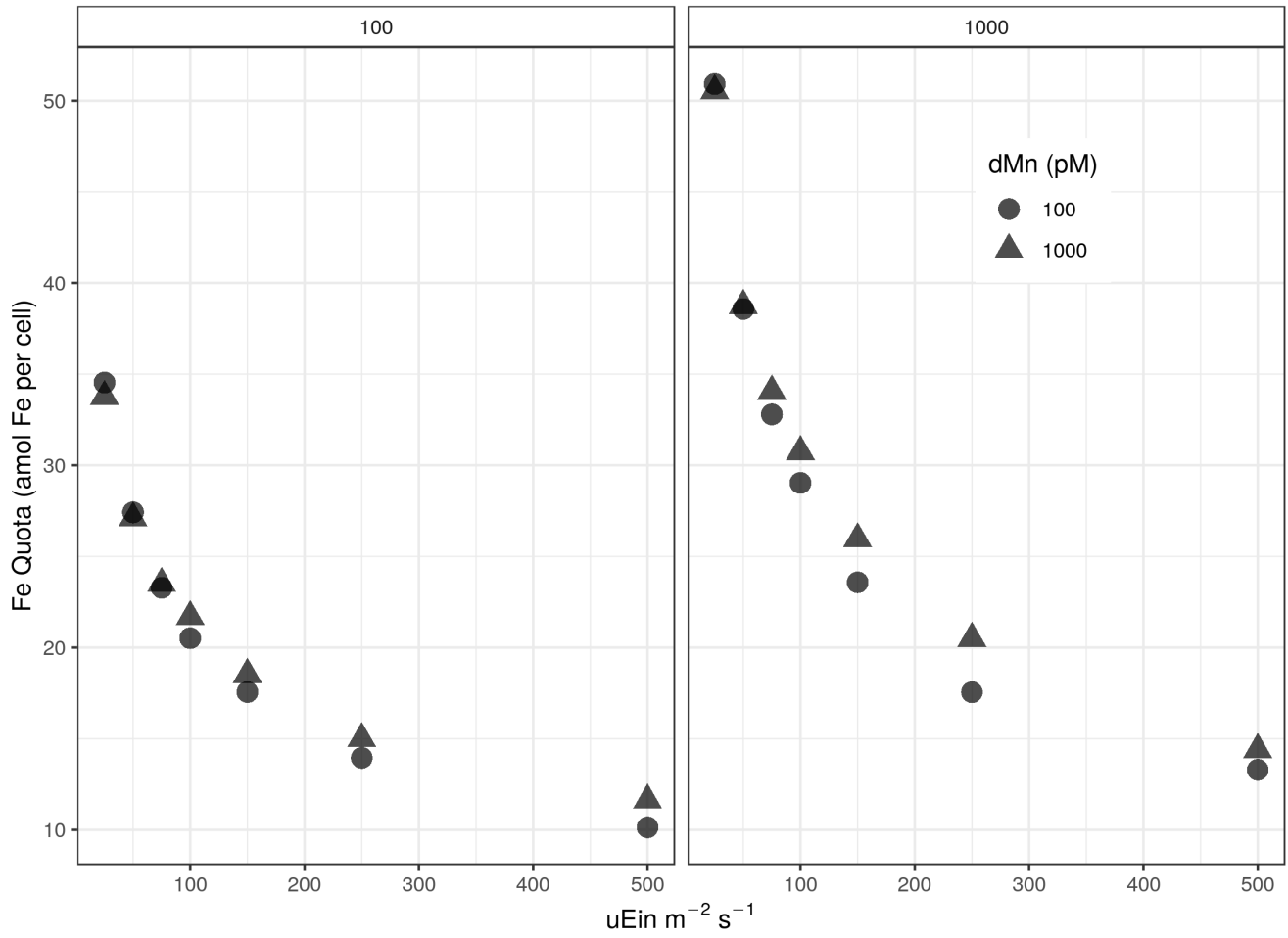
Figure S9: Light and cellular Fe quota from the cellular model have an inverse relationship. Two dFe concentrations (100 and 1000 pM) are shown (left and right panels), with two concentrations of dMn (100 and 1000 pM), across a range of light levels.
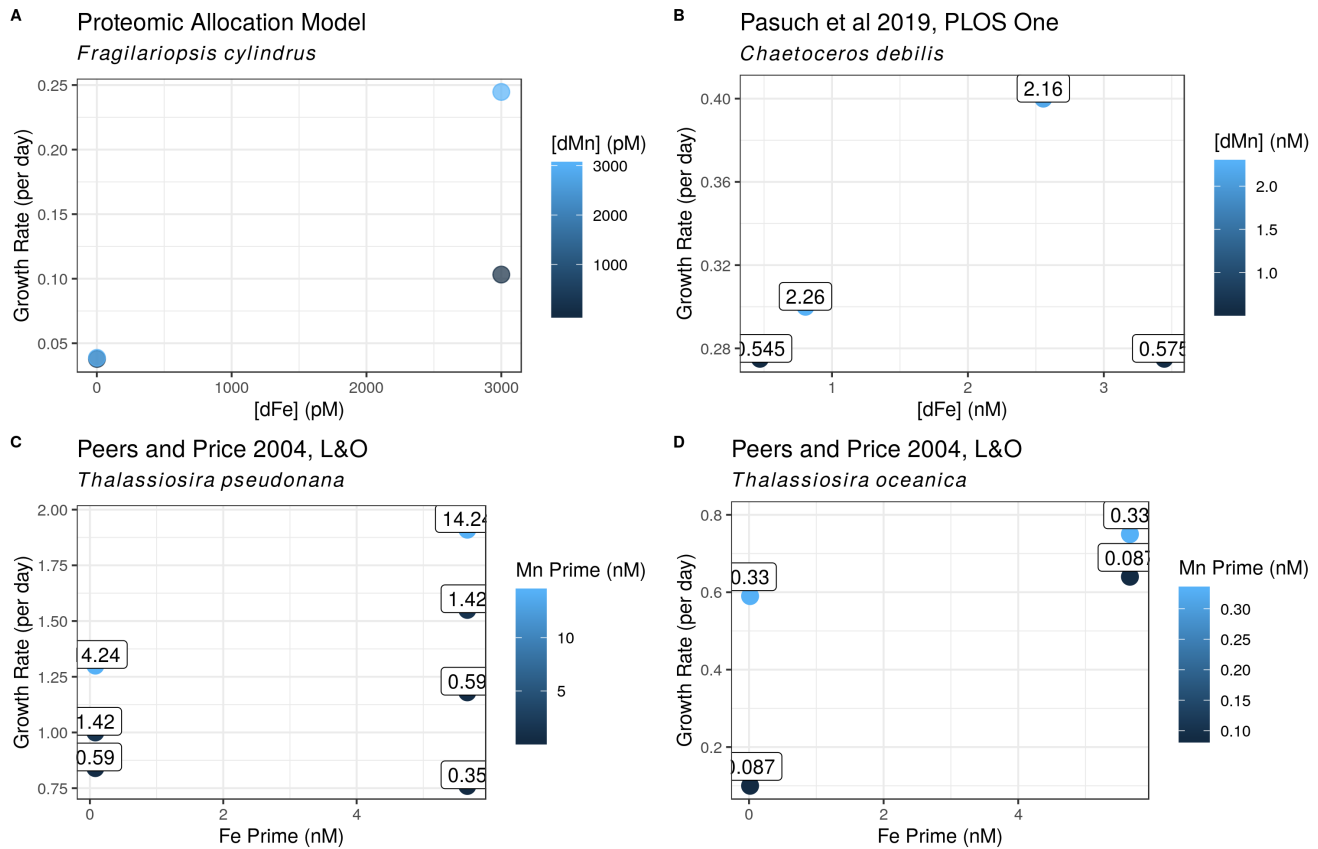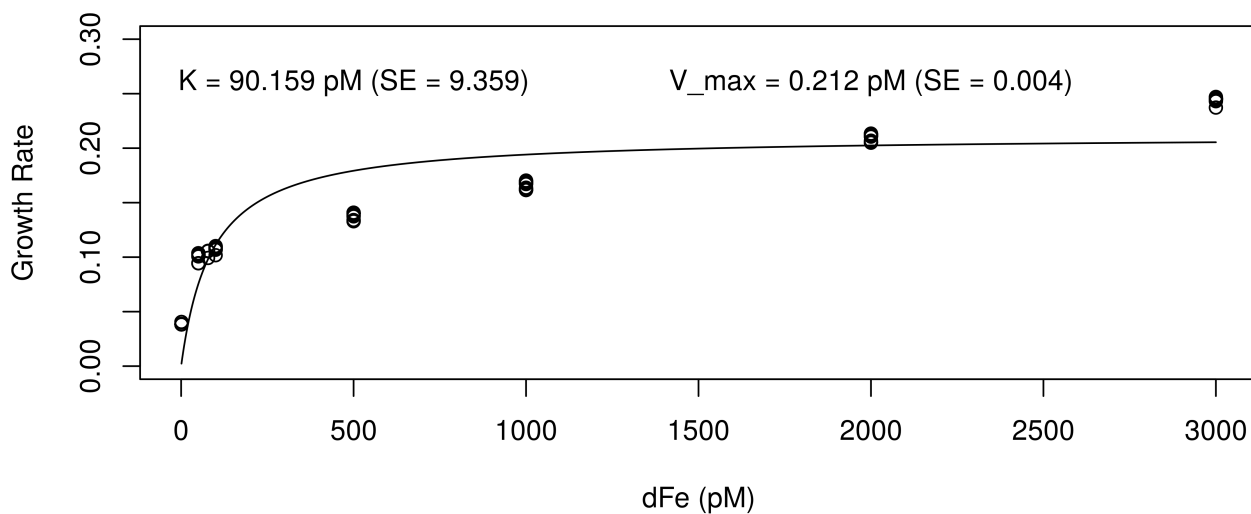
Figure S10: Model (**A**) and culture (**B-D**) growth rates under low and high Fe and low and high Mn. Manganese concentrations are given as the colour of the points (and the labels on the points). The proteomic allocation model and two datasets support the conclusion that Mn has a bigger impact on growth rate under high Fe than under low Fe (*119, 33*).

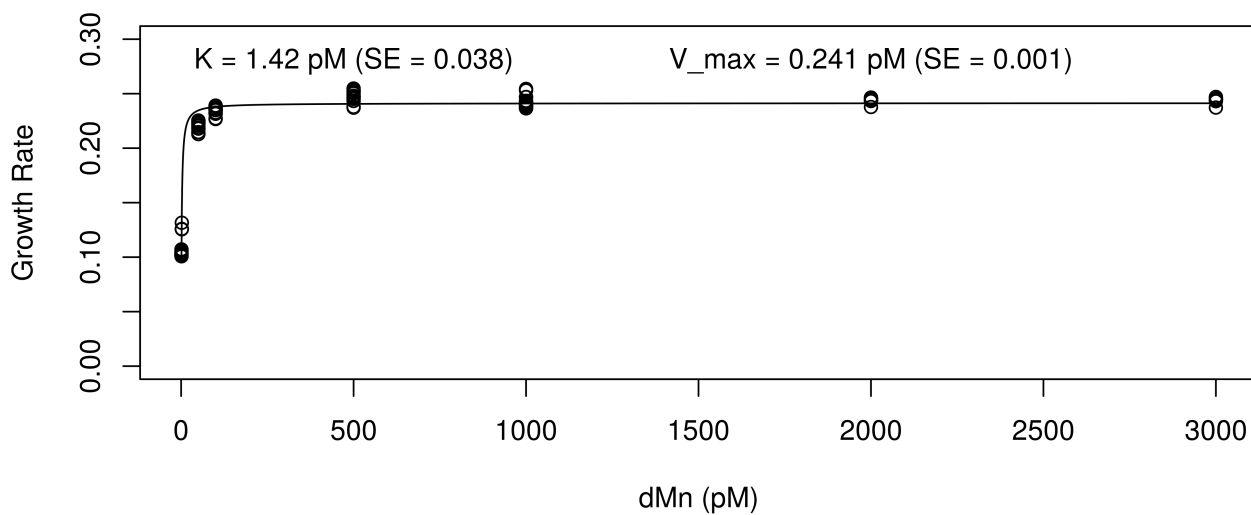Figure S11: Monod growth kinetics for dFe and dMn. Inset parameter values were found using nonlinear-least squares. For both Fe and Mn (top and bottom, respectively), saturating concentrations of the non-varying nutrient were used (saturating concentrations = 3000pM). Monod-type functions fit dMn well, but dFe poorly, but this approach was used to simply choose concentrations for testing parameter changes.

Figure S12: Change in growth rate under four different concentrations of dMn and dFe. Concentrations were chosen using Monod-functions, with the 'Low' value as the half saturation constant, and the 'High' value as an arbitrarily high, saturating, concentration (3000 pM). Parameter values were multiplied by a factor of five, and the resulting growth rate after three replicate model runs was then divided by the base model (no parameters altered). *Note that the 'Fixed Proteome Percentage' parameter was divided by five, not multiplied, because the base value is 20%.
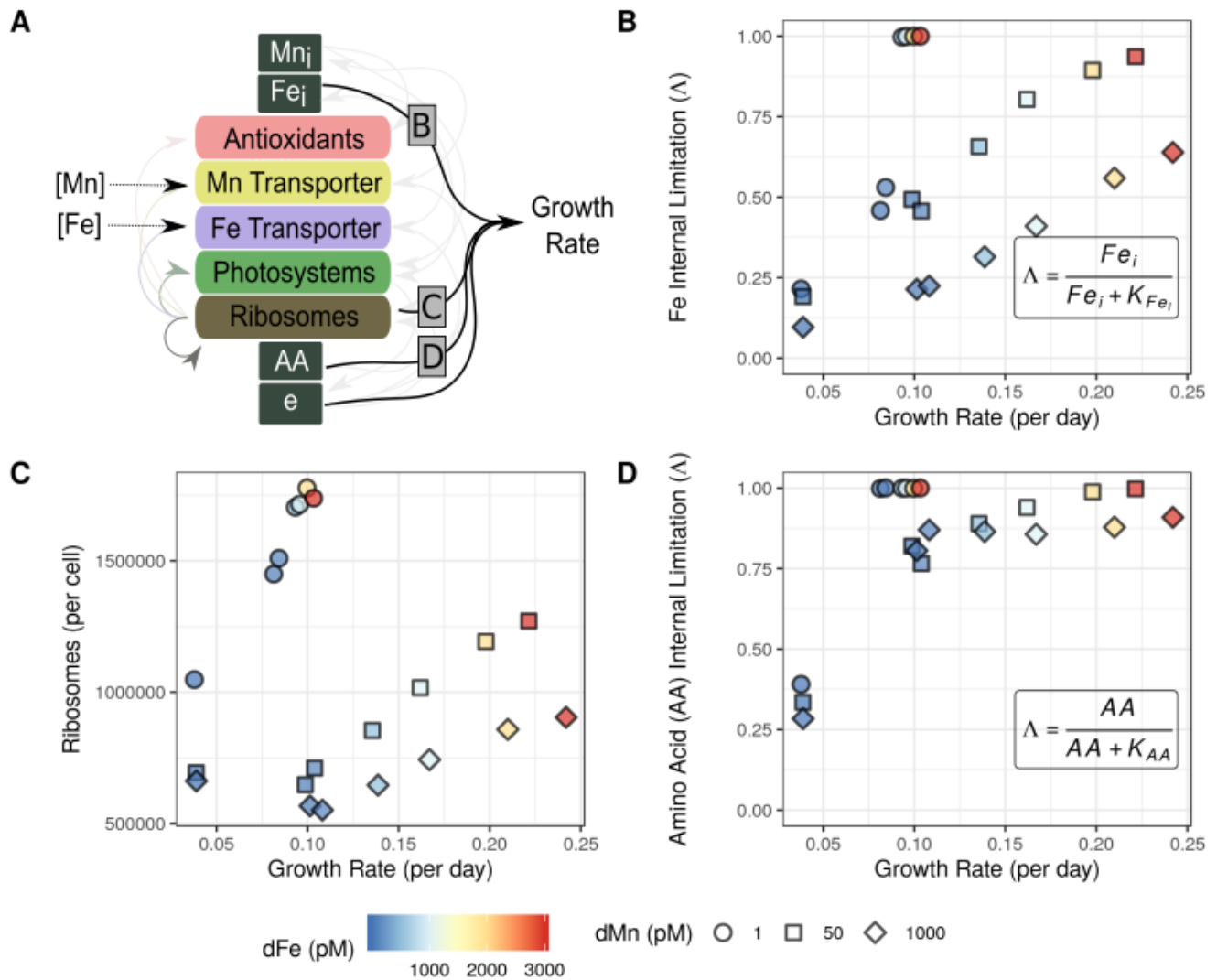
Figure S13: Extended version of additional internal cellular processes that are the proximate causes of growth rate. (**A**), the internal, modelled processes directly inhibiting growth vary across iron and manganese concentrations. (**B**), internal limitation proxy of iron varies across the growth rate and external concentration of manganese (dFe ranges from 1 pM to 3 nM, three dissolved Mn levels are shown: 1, 50, and 1000 pM). Internal Fe status (inset equation) influences the synthesis of proteins in the nitrogen metabolism pathway. (**C**), variation in ribosomes per cell with growth rate, (**D**), the total amount of available amino acids (inset equation) impacts the growth rate.
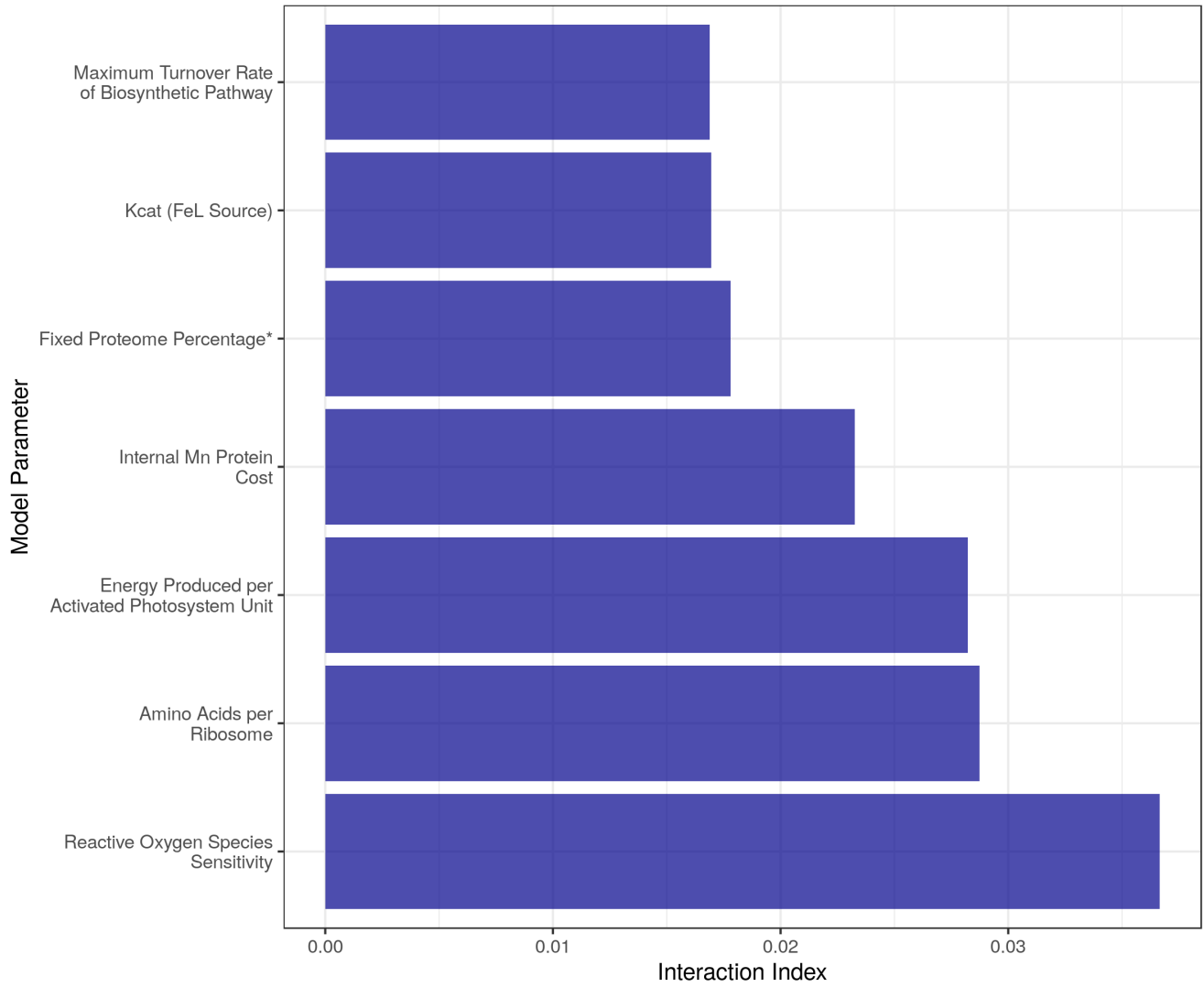
Figure S14: A parameter-specific interaction index based on the influence a parameter perturbation had on growth rate under high and low dMn and dFe concentrations (the same conditions in Fig. 2a; description of interaction index equation in the Methods). Shown here are the parameters from the proteomic allocation model with the highest interaction index (top 20%).
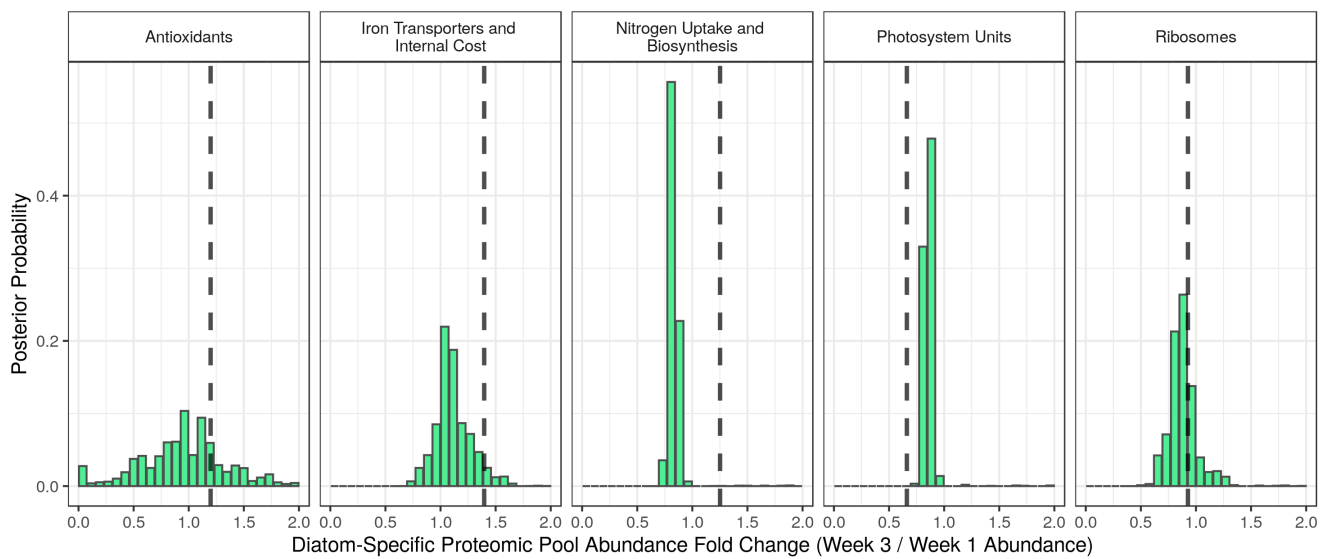
Figure S15: Posterior probability distributions of fold change from two weeks of diatom protein expression, inferred from a metaproteome. Week 1 corresponds with higher Fe and Mn, and Week 3 corresponds with lower Fe and Mn. Five of six protein pools are shown, with model posterior probability distributions given as green histograms (Mn transporters were not observed from the metaproteome). The empirical observations are shown as grey, vertical dashed lines.

Figure S16: Graphical description of transformations for calculating the protein synthesis penalty, specifically described in Equations 17–19. Panel **A** shows equation 17 and 18, while panel **B** shows equation 19 graphically.

REFERENCES AND NOTES

1. C. B. Field, M. J. Behrenfeld, J. T. Randerson, P. Falkowski, Primary production of the biosphere: Integrating terrestrial and oceanic components. *Science* **281**, 237–240 (1998).
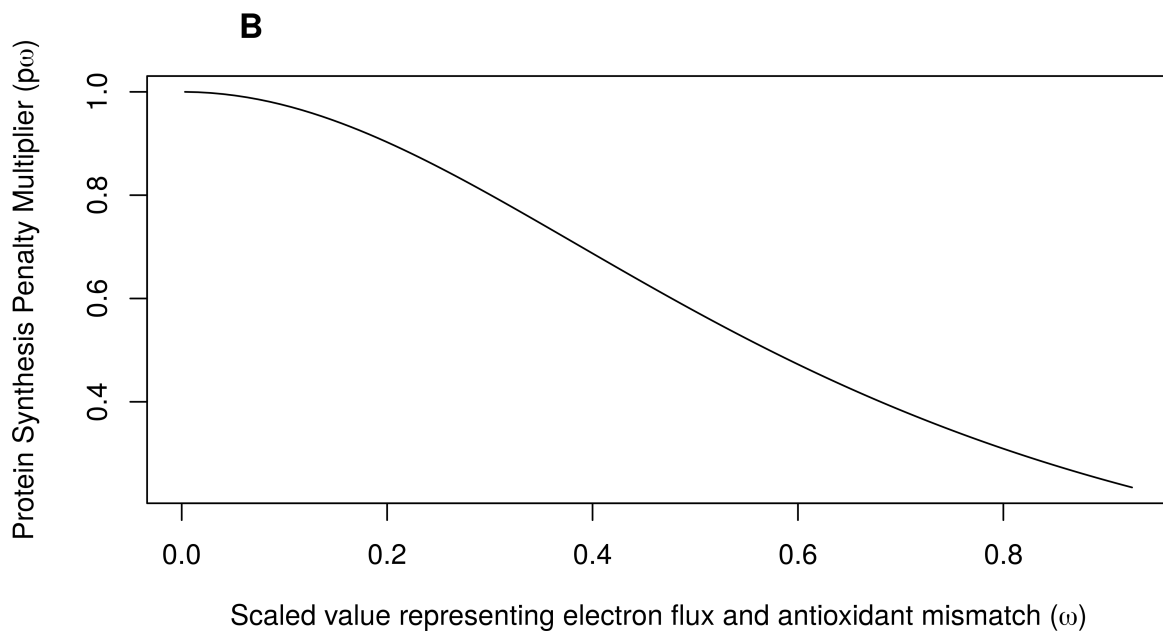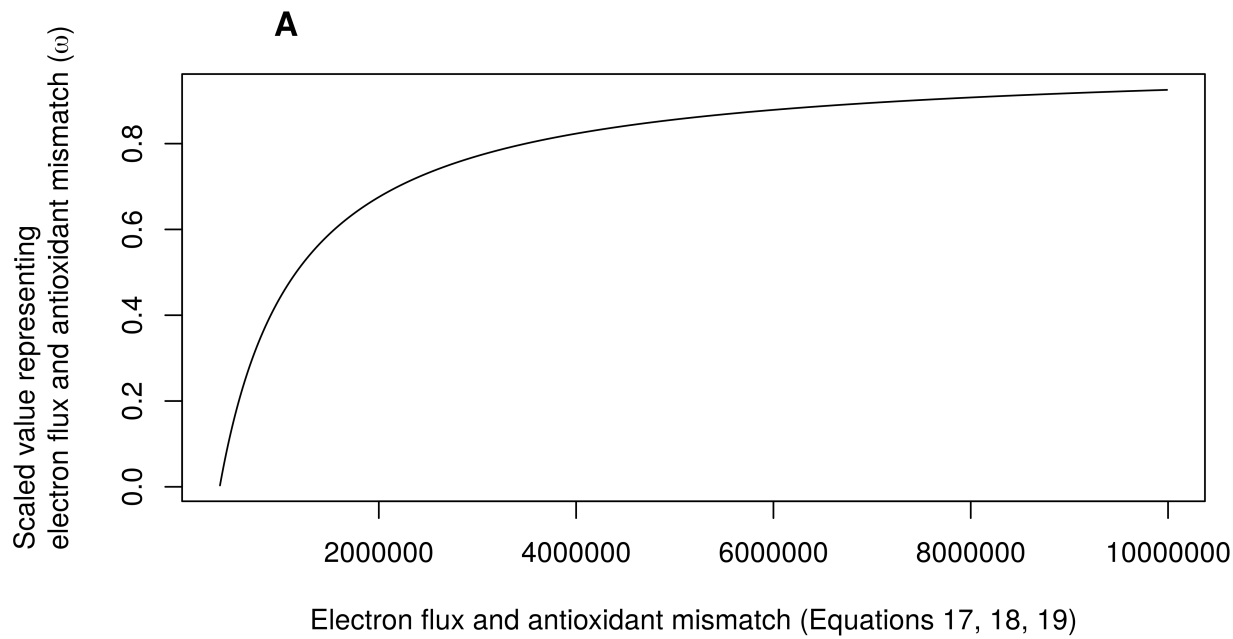
2. A. Tagliabue, A. R. Bowie, P. W. Boyd, K. N. Buck, K. S. Johnson, M. A. Saito, The integral role of iron in ocean biogeochemistry. *Nature* **543**, 51–59 (2017).

3. A. Tagliabue, N. Barrier, H. du Pontavice, L. Kwiatkowski, O. Aumont, L. Bopp, W. W. L. Cheung, D. Gascuel, O. Maury, An iron cycle cascade governs the response of equatorial Pacific ecosystems to climate change. *Glob. Chang. Biol.* **26**, 6168–6179 (2020).

4. P. Assmy, V. Smetacek, M. Montresor, C. Klaas, J. Henjes, V. H. Strass, J. M. Arrieta, U. Bathmann, G. M. Berg, E. Breitbarth, B. Cisewski, L. Friedrichs, N. Fuchs, G. J. Herndl, S. Jansen, S. Kragefsky, M. Latasa, I. Peeken, R. Rottgers, R. Scharek, S. E. Schuller, S. Steigenberger, A. Webb, D. Wolf-Gladrow, Thick-shelled, grazer-protected diatoms decouple ocean carbon and silicon cycles in the iron-limited Antarctic Circumpolar Current. *Proc. Natl. Acad. Sci.* **110**, 20633–20638 (2013).

5. B. S. Twining, S. B. Baines, The trace metal composition of marine phytoplankton. *Annu. Rev. Mar. Sci.* **5**, 191–215 (2013).

6. M. A. Saito, T. J. Goepfert, J. T. Ritt, Some thoughts on the concept of colimitation: Three definitions and the importance of bioavailability. *Limnol. Oceanogr. Lett.* **53**, 276–290 (2008).

7. M. Kafri, E. Metzl-Raz, G. Jona, N. Barkai, The cost of protein production. *Cell Rep.* **14**, 22–31 (2016).

8. E. Dekel, U. Alon, Optimality and evolutionary tuning of the expression level of a protein. *Nature* **436**, 588–592 (2005).

9. M. Basan, S. Hui, H. Okano, Z. Zhang, Y. Shen, J. R. Williamson, T. Hwa, Overflow metabolism in *Escherichia coli* results from efficient proteome allocation. *Nature* **528**, 99–104 (2015).

10. M. Jahn, V. Vialas, J. Karlsen, G. Maddalo, F. Edfors, B. Forsström, M. Uhlén, L. Käll, E. P. Hudson, Growth of cyanobacteria is constrained by the abundance of light and carbon assimilation proteins. *Cell Rep.* 478–486.e8 (2018).

11. M. Szenk, K. A. Dill, A. M. de Graff, Why do fast-growing bacteria enter overflow metabolism? Testing the membrane real estate hypothesis. *Cell Syst.* **5**, 95–104 (2017).

12. M. Schaechter, O. Maaloe, N. O. Kjeldgaard, Dependency on medium and temperature of cell size and chemical composition during balanced growth of Salmonella typhimurium. *J. Gen. Microbiol.* **19**, 592–606 (1958).

13. M. Scott, C. W. Gunderson, E. M. Mateescu, Z. Zhang, T. Hwa, *Science* **330**, 1099 (2010), 1102, Interdependence of cell growth and gene expression: Origins and consequences.

14. S. H.-J. Li, Z. Li, J. O. Park, C. G. King, J. D. Rabinowitz, N. S. Wingreen, Z. Gitai, *Escherichia coli* translation strategies differ across carbon, nitrogen, and phosphorus limitation conditions. *Nat. Microbiol.* **3**, 939–947 (2018).

15. T. J. Browning, E. P. Achterberg, I. Rapp, A. Engel, E. M. Bertrand, A. Tagliabue, C. M. Moore, Nutrient co-limitation at the boundary of an oceanic gyre. *Nature* **551**, 242–246 (2017).

16. J. K. Moore, S. C. Doney, K. Lindsay, Upper ocean ecosystem dynamics and iron cycling in a global three-dimensional model. *Glob. Biogeochem. Cycles* **18**, GB4028 (2004).

17. C. Laufkötter, M. Vogt, N. Gruber, M. Aita-Noguchi, O. Aumont, L. Bopp, E. T. Buitenhuis, S. C. Doney, J. P. Dunne, T. Hashioka, J. Hauck, T. Hirata, J. G. John, C. L. Quéré, I. D. Lima, Hideyuki Nakano Roland Séférian, I. J. Totterdell, M. Vichi, C. Völker, Drivers and uncertainties of future global marine primary production in marine ecosystem models. *Biogeosciences* **12**, 6955–6984 (2015).

18. A. Toseland, S. J. Daines, J. R. Clark, A. Kirkham, J. Strauss, C. Uhlig, T. M. Lenton, K. Valentin, G. A. Pearson, V. Moulton, T. Mock, The impact of temperature on marine phytoplankton resource allocation and metabolism. *Nat. Clim. Chang.* **3**, 979–984 (2013).

19. I. Loladze, J. J. Elser, The origins of the Redfield nitrogen-to-phosphorus ratio are in a homoeostatic protein-to-rRNA ratio. *Ecol. Lett.* **14**, 244–250 (2011).

20. J. A. Bonachela, S. D. Allison, A. C. Martiny, S. A. Levin, A model for variable phytoplankton stoichiometry based on cell protein regulation. *Biogeosciences* **10**, 4341–4356 (2013).

21. D. Talmy, J. Blackford, N. J. Hardman-Mountford, A. J. Dumbrell, R. J. Geider, An optimality model of photoadaptation in contrasting aquatic light regimes. *Limnol. Oceanogr.* **58**, 1802–1818 (2013).

22. D. P. Nicholson, R. H. R. Stanley, S. C. Doney, A phytoplankton model for the allocation of gross photosynthetic energy including the trade-offs of diazotrophy. *J. Geophys. Res. Biogeosci.* 1796–1816 (2018).

23. K. Inomura, C. Deutsch, S. T. Wilson, T. Masuda, E. Lawrenz, B. Lenka, R. Sobotka, J. M. Gauglitz, M. A. Saito, O. Prášil, M. J. Follows, Quantifying oxygen management and temperature and light dependencies of nitrogen fixation by crocosphaera watsonii. *mSphere* **4**, e00531-19 (2019).

24. T. Mock, R. P. Otillar, J. Strauss, M. McMullan, P. Paajanen, J. Schmutz, A. Salamov, R. Sanges, A. Toseland, B. J. Ward, A. E. Allen, C. L. Dupont, S. Frickenhaus, F. Maumus, A. Veluchamy, T. Wu, K. W. Barry, A. Falciatore, M. I. Ferrante, A. E. Fortunato, G. Glöckner, A. Gruber, R. Hipkin, M. G. Janech, P. G. Kroth, F. Leese, E. A. Lindquist, B. R. Lyon, J. Martin, C. Mayer, M. Parker, H. Quesneville, J. A. Raymond, C. Uhlig, R. E. Valas, K. U. Valentin, A. Z. Worden, E. V. Armbrust, M. D. Clark, C. Bowler, B. R. Green, V. Moulton, C. van Oosterhout, I. V. Grigoriev, Evolutionary genomics of the cold-adapted diatom *Fragilariopsis cylindrus*. *Nature* **541**, 536–540 (2017).

25. M. Faizi, T. Zavřel, C. Loureiro, J. Červený, R. Steuer, A model of optimal protein allocation during phototrophic growth. *Biosystems* **166**, 26–36 (2018).

26. A. G. J. Buma, H. J. W. D. Baar, R. F. Nolting, A. J. V. Bennekom, Metal enrichment experiments in the Weddell-Scotia Seas: Effects of iron and manganese on various plankton communities. *Limnol. Oceanogr.* **36**, 1865–1878 (1991).

27. T. J. Browning, H. A. Bouman, G. M. Henderson, T. A. Mather, D. M. Pyle, C. Schlosser, E. M. S. Woodward, C. M. Moore, Strong responses of Southern Ocean phytoplankton communities to volcanic ash. *Geophys. Res. Lett.* **41**, 2851–2857 (2014).

28. M. Wu, J. S. P. McCain, E. Rowland, R. Middag, M. Sandgren, A. E. Allen, E. M. Bertrand, Manganese and iron deficiency in Southern Ocean *Phaeocystis antarctica* populations revealed through taxon-specific protein indicators. *Nat. Commun.* **10**, 3582 (2019).

29. D. Molenaar, R. van Berlo, D. de Ridder, B. Teusink, Shifts in growth strategies reflect tradeoffs in cellular economics. *Mol. Syst. Biol.* **5**, 323 (2009).

30. A. Y. Weiße, D. A. Oyarzún, V. Danos, P. S. Swain, Mechanistic links between cellular trade-offs, gene expression, and growth. *Proc. Natl. Acad. Sci.* **112**, E1038–E1047 (2015).

31. T. Zavřel, M. Faizi, C. Loureiro, G. Poschmann, K. Stühler, M. Sinetova, A. Zorina, R. Steuer, J. Červený, Quantitative insights into the cyanobacterial cell economy. *eLife* **8**, e42508 (2019).

32. K. K. Niyogi, Photoprotection revisited: Genetic and molecular approaches. *Annu. Rev. Plant Biol.* **50**, 333–359 (1999).

33. G. Peers, N. M. Price, A role for manganese in superoxide dismutases and growth of iron-deficient diatoms. *Limnol. Oceanogr.* **49**, 1774–1783 (2004).

34. H. Lis, Y. Shaked, C. Kranzler, N. Keren, F. M. Morel, Iron bioavailability to phytoplankton: An empirical approach. *ISME J.* **9**, 1003–1013 (2015).

35. A. Marchetti, M. S. Parker, L. P. Moccia, E. O. Lin, A. L. Arrieta, F. Ribalet, M. E. P. Murphy, M. T. Maldonado, E. V. Armbrust, Ferritin is used for iron storage in bloom-forming marine pennate diatoms. *Nature* **457**, 467–470 (2009).

36. D. L. Aksnes, J. K. Egge, A theoretical model for nutrient uptake in phytoplankton. *Mar. Ecol. Prog. Ser.* **70**, 65–72 (1991).

37. D. L. Aksnes, F. J. Cao, Inherent and apparent traits in microbial nutrient uptake. *Mar. Ecol. Prog. Ser.* **440**, 41–51 (2011).

38. Ø. Fiksen, M. J. Follows, D. L. Aksnes, Trait-based models of nutrient uptake in microbes extend the Michaelis-Menten framework. *Limnol. Oceanogr.* **58**, 193–202 (2013).

39. R. D. Wilkinson, Approximate Bayesian computation (ABC) gives exact results under the assumption of model error. *Stat. Appl. Genet. Mol. Biol.* **12**, 129–141 (2013).

40. L. Jabre, A. E. Allen, J. Scott P. Mc Cain, John P. Mc Crow, N. Tenenbaum, J. L. Spackeen, R. E. Sipler, B. R. Green, D. A. Bronk, D. A. Hutchins, E. M. Bertrand, Molecular underpinnings and biogeochemical consequences of enhanced diatom growth in a warming Southern Ocean. *bioRxiv*, 2020.07.01.177865 (2020).

41. E. M. Bertrand, J. P. McCrow, A. Moustafa, H. Zheng, J. B. McQuaid, T. O. Delmont, A. F. Post, R. E. Sipler, J. L. Spackeen, K. Xu, D. A. Bronk, D. A. Hutchins, A. E. Allen, Phytoplankton–bacterial interactions mediate micronutrient colimitation at the coastal Antarctic sea ice edge. *Proc. Natl. Acad. Sci.* **112**, 9938–9943 (2015).

42. M. Kleiner, E. Thorson, C. E. Sharp, X. Dong, D. Liu, C. Li, M. Strous, Assessing species biomass contributions in microbial communities via metaproteomics. *Nat. Commun.* **8**, 1558 (2017).

43. J. S. P. McCain, E. M. Bertrand, Prediction and consequences of cofragmentation in metaproteomics. *J. Proteome Res.* **18**, 3555–3566 (2019).

44. N. R. Cohen, W. Gong, D. M. Moran, M. R. McIlvin, M. A. Saito, A. Marchetti, Transcriptomic and proteomic responses of the oceanic diatom *Pseudo-nitzschia granii* to iron limitation. *Environ. Microbiol.* **20**, 3109–3126 (2018).

45. B. L. Nunn, J. F. Faux, A. A. Hippmann, M. T. Maldonado, H Rodger Harvey, D. R. Goodlett, P. W. Boyd, R. F. Strzepek, Diatom proteomics reveals unique acclimation strategies to mitigate Fe limitation. *PLOS ONE* **8**, e75653 (2013).

46. L. Jabre, E. M. Bertrand, Interactive effects of iron and temperature on the growth of *Fragilariopsis cylindrus*. *Limnol. Oceanogr. Lett.* **5**, 363–370 (2020).

47. B. S. Twining, S. B. Baines, N. S. Fisher, Element stoichiometries of individual plankton cells collected during the Southern Ocean Iron Experiment (SOFeX). *Limnol. Oceanogr.* **49**, 2115–2128 (2004).

48. J. B. McQuaid, A. B. Kustka, M. Oborník, A. Horák, J. P. McCrow, B. J. Karas, H. Zheng, T. Kindeberg, A. J. Andersson, K. A. Barbeau, A. E. Allen, Carbonate-sensitive phytotransferrin controls high-affinity iron uptake in diatoms. *Nature* **555**, 534–537 (2018).

49. W. Sunda, S. Huntsman, Regulation of cellular manganese and manganese transport rates in the unicellular alga Chlamydomonas1. *Limnol. Oceanogr.* **30**, 71–80 (1985).

50. W. G. Sunda, S. A. Huntsman, Interrelated influence of iron, light and cell size on marine phytoplankton growth. *Nature* **2051**, 389 (1997).

51. C. Waldron, F. Lacroute, Effect of growth rate on the amounts of ribosomal and transfer ribonucleic acids in yeast. *J. Bacteriol.* **122**, 855–865 (1975).

52. C. M. Moore, M. M. Mills, K. R. Arrigo, I. Berman-Frank, L. Bopp, P. W. Boyd, E. D. Galbraith, R. J. Geider, C. Guieu, S. L. Jaccard, T. D. Jickells, J. la Roche, T. M. Lenton, N. M. Mahowald, E. Marañón, I. Marinov, J. K. Moore, T. Nakatsuka, A. Oschlies, M. A. Saito, T. F. Thingstad, A. Tsuda, O. Ulloa, Processes and patterns of oceanic nutrient limitation. *Nat. Geosci.* **6**, 701–710 (2013).

53. J. J. Elser, D. R. Dobberfuhl, N. A. MacKay, J. H. Schampel, Organism size, life history, and N:P stoichiometry. *Bioscience* **46**, 674–684 (1996).

54. G. Parker, J. M. Smith, Optimality theory in evolutionary biology. *Nature* **348**, 27–33 (1990).

55. S. Mishra, J. Imlay, Why do bacteria use so many enzymes to scavenge hydrogen peroxide?. *Arch. Biochem. Biophys.* **525**, 145–160 (2012).

56. M. R. Droop, The nutrient status of algal cells in continuous culture. *J. Mar. Biol. Assoc. UK* **9**, 825–855 (1974).

57. W. S. Harpole, J. T. Ngai, E. E. Cleland, E. W. Seabloom, E. T. Borer, M. E. S. Bracken, J. J. Elser, D. S. Gruner, H. Hillebrand, J. B. Shurin, J. E. Smith, Nutrient co-limitation of primary producer communities. *Ecol. Lett.* **14**, 852–862 (2011).

58. S. L. Deppeler, A. T. Davidson, Southern ocean phytoplankton in a changing climate. *Front. Mar. Sci.* **4**, 40 (2017).

59. R. W. Holton, H. H. Blecker, M. Onorb, Effect of growth temperature on the fatty acid composition of a blue-green alga. *Phytochemistry* **3**, 595–602 (1964).

60. N. A. Held, E. A. Webb, M. M. McIlvin, D. A. Hutchins, N. R. Cohen, D. M. Moran, K. Kunde, M. C. Lohan, C. Mahaffey, E. M. S. Woodward, M. A. Saito, Co-occurrence of Fe and P stress in natural populations of the marine diazotroph *Trichodesmium*;. *Biogeosciences* **17**, 2537–2551 (2020).

61. N. M. Levine, K. Zhang, M. Longo, A. Baccini, O. L. Phillips, S. L. Lewis, E. Alvarez-Dávila, A. C. Segalin de Andrade, R. J. W. Brienen, T. L. Erwin, T. R. Feldpausch, A. L. Monteagudo Mendoza, P. Nuñez Vargas, A. Prieto, J. E. Silva-Espejo, Y. Malhi, P. R. Moorcroft, Ecosystem heterogeneity determines the ecological resilience of the Amazon to climate change. *Proc. Natl. Acad. Sci.* **113**, 793–797 (2016).

62. B.-P. Han, Photosynthesis–irradiance response at physiological level: A mechanistic model. *J. Theor. Biol.* **213**, 121–127 (2001).

63. H. C. Berg, E. M. Purcell, Physics of chemoreception. *Biophys. J.* **20**, 193–219 (1977).

64. R. Zwanzig, Diffusion-controlled ligand binding to spheres partially covered by receptors: An effective medium treatment. *Proc. Natl. Acad. Sci.* **87**, 5856–5857 (1990).

65. J. A. Bonachela, M. Raghib, S. A. Levin, Dynamic model of flexible phytoplankton nutrient uptake. *Proc. Natl. Acad. Sci.* **108**, 20633–20638 (2011).

66. C. Völker, D. A. Wolf-Gladrow, Physical limits on iron uptake mediated by siderophores or surface reductases. *Mar. Chem.* **65**, 227–244 (1999).

67. H. Ploug, W. Stolte, B. B. Jørgensen, Diffusive boundary layers of the colony-forming plankton alga *Phaeocystis* sp.—Implications for nutrient uptake and cellular growth. *Limnol. Oceanogr.* **44**, 1959–1967 (1999).

68. R. Kadner, Cytoplasmic membrane, in *Escherichia coli and Salmonella: Cellular and Molecular Biology* (The American Society for Microbiology, ed. 2, 1996).

69. Y. Saito, A theoretical study on the diffusion current at the stationary electrodes of circular and narrow band types. *Rev. Polarogr.* **15**, 177–187 (1968).

70. R. J. Hudson, F. M. Morel, lron transport in marine phytoplankton: Kinetics of cellular and medium coordination reactions. *Limnol. Oceanogr.* **35**, 1002–1020 (1990).

71. W. G. Sunda, S. A. Huntsman, Iron uptake and growth limitation in oceanic and coastal phytoplankton. *Mar. Chem.* **50**, 189–206 (1995).

72. Y. Shaked, A. B. Kustka, M. M. Morel, A general kinetic model for iron acquisition by eukaryotic phytoplankton. *Limnol. Oceanogr.* **50**, 872–882 (2005).

73. M. Gledhill, K. N. Buck, The organic complexation of iron in the marine environment: A review. *Front. Microbiol.* **3**, 69 (2012).

74. Y. Shaked, H. Lis, Disassembling iron availability to phytoplankton. *Front. Microbiol.* **3**, 123 (2012).

75. Y. Shaked, K. N. Buck, T. Mellett, M. T. Maldonado, Insights into the bioavailability of oceanic dissolved Fe from phytoplankton uptake kinetics. *ISME J.* **14**, 1182–1193 (2020).

76. Y. Nishiyama, S. I. Allakhverdiev, N. Murata, Protein synthesis is the primary target of reactive oxygen species in the photoinhibition of photosystem II. *Physiol. Plant.* **142**, 35–46 (2011).

77. Z. V. Finkel, M. J. Follows, A. J. Irwin, Size-scaling of macromolecules and chemical energy content in the eukaryotic microalgae. *J. Plankton Res.* **38**, 1151–1162 (2016).

78. S. Hui, J. M. Silverman, S. S. Chen, D. W. Erickson, M. Basan, J. Wang, T. Hwa, J. R. Williamson, Quantitative proteomic analysis reveals a simple strategy of global resource allocation in bacteria. *Mol. Syst. Biol.* **11**, 784 (2015).

79. E. Metzl-Raz, M. Kafri, G. Yaakov, I. Soifer, Y. Gurvich, N. Barkai, Principles of cellular resource allocation revealed by condition-dependent proteome profiling. *eLife* **6**, e28034 (2017).

80. S. Menden-Deuer, E. J. Lessard, Carbon to volume relationships for dinoflagellates, diatoms, and other protist plankton. *Limnol. Oceanogr.* **45**, 569–579 (2000).

81. A. L. Manuell, K. Yamaguchi, P. A. Haynes, R. A. Milligan, S. P. Mayfield, Composition and structure of the 80S ribosome from the green alga *Chlamydomonas reinhardtii*: 80S ribosomes are conserved in plants and animals. *J. Mol. Biol.* **351**, 266–279 (2005).

82. F. A. Wollman, L. Minai, R. Nechushtai, The biogenesis and assembly of photosynthetic proteins in thylakoid membranes. *Biochim. Biophys. Acta Bioenerg.* **1411**, 21–85 (1999).

83. T. H. Coale, M. Moosburner, A. Horák, M. Oborník, K. A. Barbeau, A. E. Allen, Reduction-dependent siderophore assimilation in a model pennate diatom. *Proc. Natl. Acad. Sci.* **116**, 23609–23617 (2019).

84. C. E. Blaby-Haas, S. S. Merchant, Regulating cellular trace metal economy in algae. *Curr. Opin. Plant Biol.* **39**, 88–96 (2017).

85. K. Ishiyama, E. Inoue, T. Yamaya, H. Takahashi, Gln49 and Ser174 residues play critical roles in determining the catalytic efficiencies of plant glutamine synthetase. *Plant Cell Physiol.* **47**, 299–303 (2006).

86. D. K. Button, Nutrient uptake by microorganisms according to kinetic parameters from theory as related to cytoarchitecture. *Microbiol. Mol. Biol. Rev.* **62**, 636–645 (1998).

87. R. F. Strzepek, K. A. Hunter, R. D. Frew, P. J. Harrison, P. W. Boyd, Iron-light interactions differ in Southern Ocean phytoplankton. *Limnol. Oceanogr.* **57**, 1182–1200 (2012).

88. R. F. Strzepek, P. W. Boyd, W. G. Sunda, Photosynthetic adaptation to low iron, light, and temperature in Southern Ocean phytoplankton. *Proc. Natl. Acad. Sci.* **116**, 4388–4393 (2019).

89. E. P. Achterberg, T. W. Holland, A. R. Bowie, R. F. C. Mantoura, P. J. Worsfold, Determination of iron in seawater. *Anal. Chim. Acta* **442**, 1–14 (2001).

90. I. Rapp, C. Schlosser, D. Rusiecka, M. Gledhill, E. P. Achterberg, Automated preconcentration of Fe, Zn, Cu, Ni, Cd, Pb, Co, and Mn in seawater with analysis using high-resolution sector field inductively-coupled plasma mass spectrometry. *Anal. Chim. Acta* **976**, 1–13 (2017).

91. S. Kagaya, E. Maeba, Y. Inoue, W. Kamichatani, T. Kajiwara, H. Yanai, M. Saito, K. Tohda, A solid phase extraction using a chelate resin immobilizing carboxymethylated pentaethylenehexamine for separation and preconcentration of trace elements in water samples. *Talanta* **79**, 146–152 (2009).

92. R. Schlitzer, R. F. Anderson, E. M. Dodas, M. Lohan, W. Geibert, A. Tagliabue, A. Bowie, C. Jeandel, M. T. Maldonado, W. M. Landing, D. Cockwell, C. Abadie, W. Abouchami, E. P. Achterberg, A. Agather, A. Aguliar-Islas, H. M. van Aken, M. Andersen, C. Archer, M. Auro, H. J. de Baar, O. Baars, A. R. Baker, K. Bakker, C. Basak, M. Baskaran, N. R. Bates, D. Bauch, P. van Beek, M. K. Behrens, E. Black, K. Bluhm, L. Bopp, H. Bouman, K. Bowman, J. Bown, P. Boyd, M. Boye, E. A. Boyle, P. Branellec, L. Bridgestock, G. Brissebrat, T. Browning, K. W. Bruland, H. J. Brumsack, M. Brzezinski, C. S. Buck, K. N. Buck, K. Buesseler, A. Bull, E. Butler, P. Cai, P. C. Mor, D. Cardinal, C. Carlson, G. Carrasco, N. Casacuberta, K. L. Casciotti, M. Castrillejo, E. Chamizo, R. Chance, M. A. Charette, J. E. Chaves, H. Cheng, F. Chever, M. Christl, T. M. Church, I. Closset, A. Colman, T. M. Conway, D. Cossa, P. Croot, J. T. Cullen, G. A. Cutter, C. Daniels, F. Dehairs, F. Deng, H. T. Dieu, B. Duggan, G. Dulaquais, C. Dumousseaud, Y. Echegoyen-Sanz, R. L. Edwards, M. Ellwood, E. Fahrbach, J. N. Fitzsimmons, A. Russell Flegal, M. Q. Fleisher, T. van de Flierdt, M. Frank, J. Friedrich, F. Fripiat, H. Fröllje, S. J. G. Galer, T. Gamo, R. S. Ganeshram, J. Garcia-Orellana, E. Garcia-Solsona, M. Gault-Ringold, E. George, L. J. A. Gerringa, M. Gilbert, J. M. Godoy, S. L. Goldstein, S. R. Gonzalez, K. Grissom, C. Hammerschmidt, A. Hartman, C. S. Hassler, E. C. Hathorne, M. Hatta, N. Hawco, C. T. Hayes, L. E. Heimbürger, J. Helgoe, M. Heller, G. M. Henderson, P. B. Henderson, S. van Heuven, P. Ho, T. J. Horner, Y. T. Hsieh, K. F. Huang, M. P. Humphreys, K. Isshiki, J. E. Jacquot, D. J. Janssen, W. J. Jenkins, S. John, E. M. Jones, J. L. Jones, D. C. Kadko, R. Kayser, T. C. Kenna, R. Khondoker, T. Kim, L. Kipp, J. K. Klar, M. Klunder, S. Kretschmer, Y. Kumamoto, P. Laan, M. Labatut, F. Lacan, P. J. Lam, M. Lambelet, C. H. Lamborg, F. A. C. le Moigne, E. le Roy, O. J. Lechtenfeld, J. M. Lee, P. Lherminier, S. Little, M. López-Lora, Y. Lu, P. Masque, E. Mawji, C. R. Mcclain, C. Measures, S. Mehic, J. L. M. Barraqueta, P. van der Merwe, R. Middag, S. Mieruch, A. Milne, T. Minami, J. W. Moffett, G. Moncoiffe, W. S. Moore, P. J. Morris, P. L. Morton, Y. Nakaguchi, N. Nakayama, J. Niedermiller, J. Nishioka, A. Nishiuchi, A. Noble, H. Obata, S. Ober, D.

C. Ohnemus, J. van Ooijen, J. O'Sullivan, S. Owens, K. Pahnke, M. Paul, F. Pavia, L. D. Pena, B. Peters, F. Planchon, H. Planquette, C. Pradoux, V. Puigcorbé, P. Quay, F. Queroue, A. Radic, S. Rauschenberg, M. Rehkämper, R. Rember, T. Remenyi, J. A. Resing, J. Rickli, S. Rigaud, M. J. A. Rijkenberg, S. Rintoul, L. F. Robinson, M. Roca-Martí, V. Rodellas, T. Roeske, J. M. Rolison, M. Rosenberg, S. Roshan, M. M. Rutgers van der Loeff, E. Ryabenko, M. A. Saito, L. A. Salt, V. Sanial, G. Sarthou, C. Schallenberg, U. Schauer, H. Scher, C. Schlosser, B. Schnetger, P. Scott, P. N. Sedwick, I. Semiletov, R. Shelley, R. M. Sherrell, A. M. Shiller, D. M. Sigman, S. K. Singh, H. A. Slagter, E. Slater, W. M. Smethie, H. Snaith, Y. Sohrin, B. Sohst, J. E. Sonke, S. Speich, R. Steinfeldt, G. Stewart, T. Stichel, C. H. Stirling, J. Stutsman, G. J. Swarr, J. H. Swift, A. Thomas, K. Thorne, C. P. Till, R. Till, A. T. Townsend, E. Townsend, R. Tuerena, B. S. Twining, D. Vance, S. Velazquez, C. Venchiarutti, M. Villa-Alfageme, S. M. Vivancos, A. H. L. Voelker, B. Wake, M. J. Warner, R. Watson, E. van Weerlee, M. Alexandra Weigand, Y. Weinstein, D. Weiss, A. Wisotzki, E. M. S. Woodward, J. Wu, Y. Wu, K. Wuttig, N. Wyatt, Y. Xiang, R. C. Xie, Z. Xue, H. Yoshikawa, J. Zhang, P. Zhang, Y. Zhao, L. Zheng, X. Y. Zheng, M. Zieringer, L. A. Zimmer, P. Ziveri, P. Zunino, C. Zurbrick, The GEOTRACES intermediate data product 2017. *Chem. Geol.* **493**, 210–223 (2018).

93. C. de Boyer Montegut, G. Madec, A. S. Fischer, A. Lazar, D. Iudicone, Mixed layer depth over the global ocean: An examination of profile data and a profile-based climatology. *J. Geophys. Res.* **109**, C12003 (2004).

94. M. J. Behrenfeld, E. Boss, D. A. Siegel, D. M. Shea, Carbon-based ocean productivity and phytoplankton physiology from space. *Glob. Biogeochem. Cycles* **19**, GB1006 (2005).

95. H. Weisser, S. Nahnsen, J. Grossmann, L. Nilse, A. Quandt, H. Brauer, M. Sturm, E. Kenar, O. Kohlbacher, R. Aebersold, L. Malmström, An automated pipeline for high-throughput label-free quantitative proteomics. *J. Proteome Res.* **12**, 1628–1644 (2013).

96. S. Kim, P. A. Pevzner, MS-GF+ makes progress towards a universal database search tool for proteomics. *Nat. Commun.* **5**, 5277 (2014).

97. H. Weisser, J. S. Choudhary, Targeted feature detection for data-dependent shotgun proteomics. *J. Proteome Res.* **16**, 2964–2974 (2017)s.

98. M. Kanehisa, S. Goto, KEGG: Kyoto Encyclopedia of Genes and Genomes. *Nucleic Acids Res.* **28**, 27–30 (2000).

99. M. Kanehisa, Y. Sato, M. Kawashima, M. Furumichi, M. Tanabe, KEGG as a reference resource for gene and protein annotation. *Nucleic Acids Res.* **44**, D457–D462 (2016).

100. R. L. Tatusov, N. D. Fedorova, J. D. Jackson, A. R. Jacobs, B. Kiryutin, E. V. Koonin, D. M. Krylov, R. Mazumder, S. L. Mekhedov, A. N. Nikolskaya, B Sridhar Rao, S. Smirnov, A. V. Sverdlov, S. Vasudevan, Y. I. Wolf, J. J. Yin, D. A. Natale, The COG database: An updated version includes eukaryotes. *BMC Bioinformatics* **4**, 41 (2003).

101. J. Mistry, S. Chuguransky, L. Williams, M. Qureshi, G. A. Salazar, E. L. L. Sonnhammer, S. C. E. Tosatto, L. Paladin, S. Raj, L. J. Richardson, R. D. Finn, A. Bateman, Pfam: The protein families database in 2021. *Nucleic Acids Res.* **49**, D412–D419 (2021).

102. D. H. Haft, J. D. Selengut, O. White, The TIGRFAMs database of protein families. *Nucleic Acids Res.* **31**, 371–373 (2003).

103. P. Fearnhead, D. Prangle, Constructing summary statistics for approximate Bayesian computation: Semi-automatic approximate Bayesian computation. *J. R. Stat. Soc. Ser. B Stat Methodol.* **74**, 419–474 (2012).

104. A. A. Alahmadi, J. A. Flegg, D. G. Cochrane, C. C. Drovandi, J. M. Keith, A comparison of approximate versus exact techniques for Bayesian parameter inference in nonlinear ordinary differential equation models. *R. Soc. Open Sci.* **7**, 191315 (2020).

105. Y. Perez-Riverol, A. Csordas, J. Bai, M. Bernal-Llinares, S. Hewapathirana, D. J. Kundu, A. Inuganti, J. Griss, G. Mayer, M. Eisenacher, E. Pérez, J. Uszkoreit, J. Pfeuffer, T. Sachsenberg, Ş. Yılmaz, S. Tiwary, J. Cox, E. Audain, M. Walzer, A. F. Jarnuczak, T. Ternent, A. Brazma, J. A. Vizcaíno, The PRIDE database and related tools and resources in 2019: Improving support for quantification data. *Nucleic Acids Res.* **47**, D442–D450 (2019).

106. J. Raven, Predictions of Mn and Fe use efficiencies of phototrophic growth as a function of light availability for growth and of C assimilation pathway. *New Phytol.* **116**, 1–18 (1990).

107. Y. Sheng, I. A. Abreu, D. E. Cabelli, M. J. Maroney, A. F. Miller, M. Teixeira, J. S. Valentine, Superoxide dismutases and superoxide reductases. *Chem. Rev.* **114**, 3854–3918 (2014).

108. I. Lambeck, J. C. Chi, S. Krizowski, S. Mueller, N. Mehlmer, M. Teige, K. Fischer, G. Schwarz, Kinetic analysis of 14-3-3-inhibited *Arabidopsis thaliana* nitrate reductase. *Biochemistry* **49**, 8177–8186 (2010).

109. A. Hindmarsh, *ODEPACK, a Systematized Collection of ODE Solvers in Scientific Computing* (Elsevier, 1983).

110. M. Pilon, K. Ravet, W. Tapken, The biogenesis and physiological function of chloroplast superoxide dismutases. *Biochim. Biophys. Acta Bioenerg.* **1807**, 989–998 (2011).

111. K. Ogawa, S. Kanematsu, K. Takabe, K. Asada, Attachment of CuZn-superoxide dismutase to thylakoid membranes at the site of superoxide generation (PSI) in spinach chloroplasts: Detection by immuno-gold labeling after rapid freezing and substitution method. *Plant Cell Physiol.* **36**, 565–573 (1995).

112. G. Regelsberger, W. Atzenhofer, F. Rüker, G. A. Peschek, C. Jakopitsch, M. Paumann, P. G. Furtmüller, C. Obinger, Biochemical characterization of a membrane-bound manganese-containing superoxide dismutase from the cyanobacteriumanabaena PCC 7120. *J. Biol. Chem.* **277**, 43615–43622 (2002).

113. A. L. Rose, The influence of extracellular superoxide on iron redox chemistry and bioavailability. *Front. Microbiol. Chem.* **3**, 124 (2012).

114. J. M. Diaz, S. Plummer, C. M. Hansel, P. F. Andeer, M. A. Saito, M. R. McIlvin, NADPH-dependent extracellular superoxide production is vital to photophysiology in the marine diatom *Thalassiosira oceanica*. *Proc. Natl. Acad. Sci.* **116**, 16448–16453 (2019).

115. R. Middag, H. J. de Baar, P. Laan, P. H. Cai, J. C. van Ooijen, Dissolved manganese in the Atlantic sector of the Southern Ocean. *Deep-Sea Res. Part II* **58**, 2661–2677 (2011).

116. R. Sherrell, M. Lagerström, K. Forsch, S. Stammerjohn, P. Yager, Dynamics of dissolved iron and other bioactive trace metals (Mn, Ni, Cu, Zn) in the Amundsen Sea Polynya. *Elementa* **3**, 1 (2015).

117. J. A. Raven, The iron and molybdenum use efficiencies of plant growth with different energy, carbon and nitrogen sources. *New Phytol.* **109**, 279–287 (1988).

118. NASA Goddard Space Flight Center, Ocean Biology Processing Group: Sea-viewing Wide Field-of-view Sensor (SeaWiFS) Ocean Color Data, NASA OB.DAAC, Greenbelt, MD, USA. OC.2014.0, http://doi.org/10.5067/ORBVIEW-2/SEAWIFS [accessed 2 April 2019] Maintained by NA (2014).

119. F. Pausch, K. Bischof, S. Trimborn, Iron and manganese co-limit growth of the Southern Ocean diatom *Chaetoceros debilis*. *PLOS ONE* **14**, e0221959 (2019).